An ultra-high affinity synthetic nanobody blocks SARS-CoV-2 infection by locking Spike into an inactive conformation

Michael Schoof[1,2#*], Bryan Faust[1,2,3,4#], Reuben A. Saunders[1,5#], Smriti Sangwan[1,2#], Veronica Rezelj[6#], Nick Hoppe[3,4], Morgane Boone[1,2], Christian Bache Billesbølle[3,4], Marcell Zimanyi[1,2,3], Ishan Deshpande[3,4], Jiahao Liang[3], Aditya A. Anand[1,2], Niv Dobzinski[1,2], Beth Shoshana Zha[7], Benjamin Barsi-Rhyne[3], Vladislav Belyy[1,2], Andrew W. Barile-Hill[8], Sayan Gupta[9], Camille R. Simoneau[10,11,12], Kristoffer Leon[10,11,12], Kris M. White[13,14], Silke Nock[1,2], Yuwei Liu[1,2], Nevan J. Krogan[4,5,10,11], Corie Y. Ralston[9], Danielle L. Swaney[4,5,10,11], Adolfo García-Sastre[13,14], Melanie Ott[10,11,12], Marco Vignuzzi[6], QCRG Structural Biology Consortium[4], Peter Walter[1,2*], Aashish Manglik[3,4,10,15*]

[1]Howard Hughes Medical Institute, University of California at San Francisco, San Francisco, CA, USA.
[2]Department of Biochemistry and Biophysics, University of California at San Francisco, San Francisco, CA, USA.
[3]Department of Pharmaceutical Chemistry, University of California at San Francisco, San Francisco, CA, USA.
[4]Quantitative Biosciences Institute (QBI) Coronavirus Research Group Structural Biology Consortium, University of California, San Francisco, CA, USA.
[5]Department of Cellular and Molecular Pharmacology, University of California at San Francisco, San Francisco, CA, USA.
[6]Viral Populations and Pathogenesis Unit, CNRS UMR 3569, Institut Pasteur, 75724, Paris, cedex 15, France
[7]Department of Pulmonary, Critical Care, Allergy and Sleep Medicine, University of California San Francisco, San Francisco, CA 94158, USA.
[8]Cytiva Life Sciences, Marlborough, MA, USA.
[9]Molecular Biophysics and Integrated Bioimaging and the Molecular Foundry, Lawrence Berkeley National Laboratory, Berkeley, CA, USA.
[10]Quantitative Biosciences Institute (QBI), University of California San Francisco, San Francisco, CA, USA.
[11]J. David Gladstone Institutes, San Francisco, CA, USA.
[12]Department of Medicine, University of California San Francisco, San Francisco, CA, USA.
[13]Department of Microbiology, Icahn School of Medicine at Mount Sinai, New York, NY, USA.
[14]Global Health and Emerging Pathogens Institute, Icahn School of Medicine at Mount Sinai, New York, NY, USA.
[15]Department of Anesthesia and Perioperative Care, University of California at San Francisco, San Francisco, CA, USA.

[#] These authors contributed equally
* To whom correspondence should be addressed; Email: michael@walterlab.ucsf.edu, peter@walterlab.ucsf.edu, Aashish.Manglik@ucsf.edu

Abstract

Without an effective prophylactic solution, infections from SARS-CoV-2 continue to rise worldwide with devastating health and economic costs. SARS-CoV-2 gains entry into host cells via an interaction between its Spike protein and the host cell receptor angiotensin converting enzyme 2 (ACE2). Disruption of this interaction confers potent neutralization of viral entry, providing an avenue for vaccine design and for therapeutic antibodies. Here, we develop single-domain antibodies (nanobodies) that potently disrupt the interaction between the SARS-CoV-2 Spike and ACE2. By screening a yeast surface-displayed library of synthetic nanobody sequences, we identified a panel of nanobodies that bind to multiple epitopes on Spike and block ACE2 interaction via two distinct mechanisms. Cryogenic electron microscopy (cryo-EM) revealed that one exceptionally stable nanobody, Nb6, binds Spike in a fully inactive conformation with its receptor binding domains (RBDs) locked into their inaccessible down-state, incapable of binding ACE2. Affinity maturation and structure-guided design of multivalency yielded a trivalent nanobody, mNb6-tri, with femtomolar affinity for SARS-CoV-2 Spike and picomolar neutralization of SARS-CoV-2 infection. mNb6-tri retains stability and function after aerosolization, lyophilization, and heat treatment. These properties may enable aerosol-mediated delivery of this potent neutralizer directly to the airway epithelia, promising to yield a widely deployable, patient-friendly prophylactic and/or early infection therapeutic agent to stem the worst pandemic in a century.

Introduction

Over the last two decades, three zoonotic β-coronaviruses have entered the human population, causing severe respiratory symptoms with high mortality [1-3]. The ongoing COVID-19 pandemic is caused by SARS-CoV-2, the most readily transmissible of these three coronaviruses [4-7]. SARS-CoV-2 has wrecked the world's economy and societies to an unprecedented extent, to date (Aug. 3, 2020) causing 691,320 reported deaths around the globe [8]. Although public health measures have slowed its spread in many regions, infection hotspots keep reemerging. No successful vaccine or preventive treatment has yet been manufactured for any coronavirus, and the time to develop an effective and broadly available vaccine for SARS-CoV-2 remains uncertain. The development of novel therapeutic and prophylactic approaches thus remains essential, both as temporary stopgaps until an effective vaccine is generated and as permanent solutions for those segments of the population for which vaccination proves ineffective or contraindicated.

Coronavirus virions are bounded by a membrane envelope that contains ~25 copies of the homotrimeric transmembrane spike glycoprotein (Spike) responsible for virus entry into the host cell [9]. The surface-exposed portion of Spike is composed of two domains, S_1 and S_2 [10]. The S_1 domain mediates the interaction between virus and its host cell receptor, the angiotensin converting enzyme 2 (ACE2), while the S_2 domain catalyzes fusion of the viral and host cell membranes [3, 11-13]. During its biogenesis, the Spike protein is proteolytically cleaved between the S_1 and S_2 domains, which primes the virus for cellular entry [10]. Contained within S_1 is the receptor binding domain (RBD), which directly binds to ACE2. The RBD is attached to the body of Spike by a flexible region and can exist in an inaccessible down-state or an accessible up-state [14, 15]. Binding to ACE2 requires the RBD in the up-state and enables cleavage by host proteases TMPRSS2 or cathepsin, triggering a dramatic conformational change in S_2 that enables viral entry [16]. In SARS-CoV-2 virions, Spike oscillates between an active, open conformation with at least one RBD in the up-state and an inactive, closed conformation with all RBDs in the down-state [9, 11, 14, 15].

By screening a high-complexity yeast surface-displayed library of synthetic nanobodies, we have uncovered a collection of nanobodies that block the Spike-ACE2 interaction. Biochemical and structural studies revealed that two classes of these nanobodies act in distinct ways to prevent ACE2 binding. Combining affinity maturation and structure-guided multimerization, we optimized these agents and generated Spike binders that match or exceed the potency of most

monoclonal antibodies disclosed to date. Our lead neutralizing molecule, mNb6-tri, blocks SARS-CoV-2 entry in human cells at picomolar efficacy and withstands aerosolization, lyophilization, and elevated temperatures. mNb6-tri provides a promising approach to deliver a potent SARS-CoV-2 neutralizing molecule directly to the airways for prophylaxis or therapy.

Results

Synthetic nanobodies that disrupt Spike-ACE2 interaction

To isolate nanobodies that neutralize SARS-CoV-2, we screened a yeast surface-displayed library of >$2x10^9$ synthetic nanobody sequences. Our strategy was to screen for binders to the full Spike protein ectodomain, in order to capture not only those nanobodies that would compete by binding to the ACE2-binding site on the RBD directly but also those that might bind elsewhere on Spike and block ACE2 interaction through indirect mechanisms. We used a mutant form of SARS-CoV-2 Spike, Spike*, as the antigen [15]. Spike* lacks one of the two activating proteolytic cleavage sites between the S_1 and S_2 domains and introduces two mutations to stabilize the pre-fusion conformation. Spike* expressed in mammalian cells binds ACE2 with a K_D = 44 nM (Supplementary Fig. 1), consistent with previous reports [17]. Next, we labeled Spike* with biotin or with fluorescent dyes and selected nanobody-displaying yeast over multiple rounds, first by magnetic bead binding and then by fluorescence-activated cell sorting (Fig. 1A).

Three rounds of selection yielded 21 unique nanobodies that bound Spike* and showed decreased Spike* binding in the presence of ACE2. Closer inspection of their binding properties revealed that these nanobodies fall into two distinct classes. One group (Class I) binds the RBD and competes with ACE2 (Fig. 1B). A prototypical example of this class is nanobody Nb6, which binds to Spike* and to RBD alone with a K_D of 210 nM and 41 nM, respectively (Fig. 1C; Table 1). Another group (Class II), exemplified by nanobody Nb3, binds to Spike* (K_D = 61 nM), but displays no binding to RBD alone (Fig. 1C, Table 1). In the presence of excess ACE2, binding of Nb6 and other Class I nanobodies is blocked entirely, whereas binding of Nb3 and other Class II nanobodies is decreased only moderately (Fig. 1B). These results suggest that Class I nanobodies target the RBD to block ACE2 binding, whereas Class II nanobodies target other epitopes and decrease ACE2 interaction with Spike allosterically or through steric interference. Indeed, surface plasmon resonance (SPR) experiments demonstrate that Class I and Class II nanobodies can bind Spike* simultaneously (Fig. 1D).

Analysis of the kinetic rate constants for Class I nanobodies revealed a consistently greater association rate constant (k_a) for nanobody binding to the isolated RBD than to full-length Spike* (Table 1), which suggests that RBD accessibility influences the K_D. We next tested the efficacy of our nanobodies, both Class I and Class II, to inhibit binding of fluorescently labeled Spike* to ACE2-expressing HEK293 cells (Table 1, Fig. 1E). Class I nanobodies emerged with highly variable activity in this assay with Nb6 and Nb11 as two of the most potent clones with IC_{50} values of 370 and 540 nM, respectively (Table 1). For unexplained reasons, Class II nanobodies showed little to no activity in this assay (Table 1, Fig. 1E).

Going forward, we prioritized two Class I nanobodies, Nb6 and Nb11, that combine potent Spike* binding with relatively small differences in k_a between binding to Spike* or RBD. We reasoned that the epitopes recognized by Nb6 and Nb11 would be more readily accessible in the Spike protein on intact virions. For Class II nanobodies we prioritized Nb3 because of its optimal stability and yield during purification.

Nb6 and Nb11 target the RBD and directly compete with ACE2

To define the binding sites of Nb6 and Nb11, we determined their cryogenic electron microscopy (cryo-EM) structures bound to Spike* (Fig. 2A-B, Supplementary Fig. 2-4, Supplementary Table 1). Both nanobodies recognize RBD epitopes that overlap the ACE2 binding site (Fig. 2E). For Nb6 and Nb11, we resolved nanobody binding to both the open and closed conformations of Spike*. We obtained a 3.0 Å map of Nb6 bound to closed Spike*, which enabled modeling of the Nb6-Spike* complex (Fig. 2A), including the complementarity determining regions (CDRs). We also obtained lower resolution maps for Nb6 bound to open Spike* (3.8 Å), Nb11 bound to open Spike* (4.2 Å), and Nb11 bound to closed Spike* (3.7 Å). For these lower resolution maps, we could define the nanobody's binding orientation but not accurately model the CDRs.

Nb6 bound to closed Spike* straddles the interface between two adjacent RBDs. The majority of the contacting surfaces are contributed by CDR1 and CDR2 of Nb6 (Fig. 2C). CDR3 contacts the adjacent RBD that is counterclockwise positioned when viewed from the top of Spike* (Fig. 2C). The binding of one Nb6 therefore stabilizes two adjacent RBDs in the down-state. We surmise that this initial binding event pre-organizes the binding site for a second and third Nb6 molecule to stabilize the closed Spike* conformation. Indeed, binding of two Nb6 molecules would lock all three RBDs into the down-state, thus highly favoring binding of a third Nb6

because binding would not entail any further entropic cost. By contrast, Nb11 bound to down-state RBDs only contacts a single RBD (Fig. 2D).

Nb3 interacts with the Spike S_1 domain external to the RBD

Our attempts to determine the binding site of Nb3 by cryo-EM proved unsuccessful. We therefore turned to radiolytic hydroxyl radical footprinting to determine potential binding sites for Nb3. Spike*, either apo or bound to Nb3, was exposed to 5-50 milliseconds of synchrotron X-ray radiation to label solvent exposed amino acids with hydroxyl radicals. Radical-labeled amino acids were subsequently identified and quantified by mass spectrometry of trypsin/Lys-C or Glu-C protease digested Spike*[18]. Two neighboring surface residues on the S_1 domain of Spike (M177 and H207) emerged as highly protected sites in the presence of Nb3 (Supplementary Fig. 5). The degree of protection is consistent with prior observations of antibody-antigen interactions by hydroxyl radical footprinting [19]. Both M177 and H207 are greater than 40 Å distant from the ACE2 binding site on the RBD, suggesting that Nb3 may inhibit Spike-ACE2 interactions through allosteric means.

Rationally engineered multivalency increases potency

The structure of Nb6 bound to closed Spike* enabled us to engineer bivalent and trivalent nanobodies predicted to lock all RBDs in the down-state. To this end, we inserted flexible Gly-Ser linkers of either 15 or 20 amino acids to span the 52 Å distance between adjacent Nb6 monomers bound to down-state RBDs in closed Spike* (Supplementary Fig. 6). Both linker lengths are too short to span the distance (72 Å) between Nb6 bound to a down-state RBD and an up-state RBD that would co-exist in an open Spike. Moreover, binding of three RBDs in the previously reported conformation of Nb6-bound open Spike* would be physically impossible even with longer linker length because of steric clashes (Supplementary Fig. 6). By contrast, the minimum distance between adjacent Nb11 monomers bound to either open or closed Spike* is 68 Å (Supplementary Fig. 6). We therefore predicted that multivalent binding by Nb6 constructs would display significantly slowed dissociation rates due to the enhanced avidity afforded by Spike's trimeric architecture.

We assessed multivalent Nb6 binding to Spike* by SPR. Both bivalent Nb6 with a 15 amino acid linker (Nb6-bi) and trivalent Nb6 with two 20 amino acid linkers (Nb6-tri) dissociate from Spike* in a biphasic manner. The dissociation phase can be fitted to two components: a fast phase with kinetic rate constants k_{d1} of 2.7×10^{-2} s^{-1} for Nb6-bi and 2.9×10^{-2} s^{-1} for Nb6-tri, which are of the

same magnitude as that observed for monovalent Nb6 (k_d = 5.6x10^{-2} s^{-1}) and a slow phase that is dependent on avidity (k_{d2} = 3.1x10^{-4} for Nb6-bi and k_{d2} < 1.0x10^{-6} s^{-1} for Nb6-tri, respectively) (Fig. 3A). The relatively similar k_d for the fast phase suggests that a fraction of the observed binding for the multivalent constructs is nanobody binding to a single Spike* RBD. By contrast, the slow dissociation phase of Nb6-bi and Nb6-tri indicates engagement of two or three RBDs. We observed no dissociation for the slow phase of Nb6-tri over 10 minutes, indicating an upper boundary for k_{d2} of 1x10^{-6} s^{-1} and subpicomolar affinity. This measurement remains an upper-bound estimate rather than an accurate measurement because the technique is limited by the intrinsic dissociation rate of Spike* from the chip imposed by the chemistry used to immobilize Spike*.

We reasoned that the biphasic dissociation behavior could be explained by a slow interconversion between up- and down-state RBDs, with conversion to the more stable down-state required for full trivalent binding. According to this view, a single domain of Nb6-tri engaged with an up-state RBD would dissociate rapidly. The system would then re-equilibrate as the RBD flips into the down-state, eventually allowing Nb6-tri to trap all RBDs in closed Spike*. To test this notion directly, we varied the time allowed for Nb6-tri binding to Spike*. Indeed, we observed an exponential decrease in the percent fast-phase with a $t_{1/2}$ of 65 s (Fig. 3B), which, we surmise, reflects the timescale of conversion between the RBD up- and down-states in Spike*. Taken together, dimerization and trimerization of Nb6 afforded 750-fold and >200,000-fold gains in K_D, respectively.

Class I and II nanobodies prevent SARS-CoV-2 infection

We next tested the neutralization activity of trivalent versions of our top Class I (Nb6 and Nb11) and Class II (Nb3) nanobodies against SARS-CoV-2 pseudotyped lentivirus. In this assay, SARS-CoV-2 Spike is expressed as a surface protein on a lentiviral particle that contains a ZsGreen reporter gene, which is integrated and expressed upon successful viral entry into cells harboring the ACE2 receptor [20]. Nb6 and Nb11 inhibited pseudovirus infection with IC_{50} values of 2.0 μM and 2.4 μM, respectively, and Nb3 inhibited pseudovirus infection with an IC_{50} of 3.9 μM (Fig. 3C, Table 1). Nb6-tri shows a 2000-fold enhancement of inhibitory activity, with an IC_{50} of 1.2 nM, whereas trimerization of Nb11 and Nb3 resulted in more modest gains of 40- and 10-fold (51 nM and 400 nM), respectively (Fig. 3C).

We next confirmed these neutralization activities with a viral plaque assay using live SARS-CoV-2 virus infection of VeroE6 cells. Consistent with its activity against pseudotyped lentivirus, Nb6-tri proved exceptionally potent, neutralizing SARS-CoV-2 with an average IC_{50} of 160 pM (Fig. 3D). Nb3-tri neutralized SARS-CoV-2 with an average IC_{50} of 140 nM (Fig. 3D).

Affinity maturation yields a femtomolar K_D Spike inhibitor

We further optimized the potency of Nb6 by selecting high-affinity variants. To this end, we prepared a new library, starting with the Nb6 coding sequence, in which we varied each amino acid position of all three CDRs by saturation mutagenesis (Fig. 4A). After two rounds of magnetic bead-based selection, we isolated a population of high-affinity clones. Sequencing revealed two highly penetrant mutations: I27Y in CDR1 and P105Y in CDR3. We incorporated these two mutations into Nb6 to generate matured Nb6 (mNb6), which binds with 500-fold increased affinity to Spike* as measured by SPR (Fig. 4B). As a monomer, mNb6 inhibits both pseudovirus and live SARS-CoV-2 infection with low nanomolar potency, a ~200-fold improvement compared to Nb6 (Fig. 4I-J, Table 1).

A 2.9 Å cryo-EM structure of mNb6 bound to Spike* shows that, like the parent nanobody Nb6, mNb6 binds to closed Spike (Fig. 4C, Supplementary Fig. 7). The higher resolution map allowed us to build a model with high confidence and determine the effects of the I27Y and P105Y substitutions. mNb6 induces a slight rearrangement of the down-state RBDs as compared to both previously determined structures of apo-Spike* and Spike* bound to Nb6, inducing a 9° rotation of the RBD away from the central three-fold symmetry axis (Fig. 4H) [14, 15]. This deviation likely arises from a different interaction between CDR3 and Spike*, which nudges the RBDs into a new resting position. While the I27Y substitution optimizes local contacts between CDR1 in its original binding site on the RBD, the P105Y substitution leads to a marked rearrangement of CDR3 in mNb6 (Fig. 4F-G). This conformational change yields a different set of contacts between mNb6 CDR3 and the adjacent RBD (Fig. 4D). Remarkably, an X-ray crystal structure of mNb6 alone revealed dramatic conformational differences in CDR1 and CDR3 between free and Spike*-bound mNb6, suggestive of significant conformational heterogeneity for the unbound nanobodies and induced-fit rearrangements upon binding to Spike* (Fig. 4E).

The binding orientation of mNb6 is similar to that of Nb6, supporting the notion that our multivalent design would likewise enhance binding affinity. Unlike Nb6-tri, trivalent mNb6 (mNb6-tri) bound to Spike with no observable fast-phase dissociation and no measurable

dissociation over ten minutes, yielding an upper bound for the dissociation rate constant k_d of $1.0x10^{-6}$ s^{-1} ($t_{1/2}$ > 8 days) and a K_D of <1 pM (Fig. 4B). As above, more precise measurements of the dissociation rate are precluded by the surface chemistry used to immobilize Spike*.

mNb6-tri displays further gains in potency in both pseudovirus and live SARS-CoV-2 infection assays with IC_{50} values of 120 pM (5.0 ng/mL) and 54 pM (2.3 ng/mL), respectively (Fig. 4H-I, Table 1). Given the sub-picomolar affinity observed by SPR, it is likely that these viral neutralization potencies reflect the lower limit of the assays. mNb6-tri is therefore an exceptionally potent SARS-CoV-2 neutralizing antibody, among the most potent molecules disclosed to date.

Nb6, Nb6-tri, mNb6, and mNb6-tri are robust proteins

One of the most attractive properties that distinguishes nanobodies from traditional monoclonal antibodies is their extreme stability [21]. We therefore tested Nb6, Nb6-tri, mNb6, and mNb6-tri for stability regarding temperature, lyophilization, and aerosolization. Temperature denaturation experiments using circular dichroism measurements to assess protein unfolding revealed melting temperatures of 66.9, 62.0, 67.6, and 61.4 °C for Nb6, Nb6-tri, mNb6 and mNb6-tri, respectively (Fig 5A). Aerosolization and prolonged heating of Nb6, mNb6, and mNb6-tri for 1 hour at 50°C induced no loss of activity (Fig 5B). Moreover, mNb6 and mNb6-tri were stable to lyophilization and to aerosolization using a mesh nebulizer, showing no aggregation by size exclusion chromatography and preserved high affinity binding to Spike* (Fig. 5C-D).

Discussion

There is a pressing need for prophylactics and therapeutics against SARS-CoV-2 infection. Most recent strategies to prevent SARS-CoV-2 entry into the host cell aim at blocking the ACE2-RBD interaction. High-affinity monoclonal antibodies, many identified from convalescent patients, are leading the way as potential therapeutics [22-29]. While highly effective *in vitro*, these agents are expensive to produce by mammalian cell expression and need to be intravenously administered by healthcare professionals. Moreover, large doses are likely to be required for prophylactic viral neutralization, as only a small fraction of systemically circulating antibodies cross the epithelial cell layers that line the airways [30]. By contrast, single domain antibodies (nanobodies) provide significant advantages in terms of production and deliverability. They can be inexpensively produced at scale in bacteria *(E. coli)* or yeast *(P. pastoris)*.

Furthermore, their inherent stability enables aerosolized delivery directly to the nasal and lung epithelia by self-administered inhalation [31].

Monomeric mNb6 is among the most potent single domain antibodies neutralizing SARS-CoV-2 discovered to date. Multimerization of single domain antibodies has been shown to improve target affinity by avidity [31, 32]. In the case of Nb6 and mNb6, however, our design strategy enabled a multimeric construct that simultaneously engages all three RBDs, yielding profound gains in potency. Furthermore, because RBDs must be in the up-state to engage with ACE2, conformational control of RBD accessibility can serve as an added neutralization mechanism. Indeed, our Nb6-tri and mNb6-tri molecules were designed with this functionality in mind. Thus, when mNb6-tri engages with Spike, it prevents ACE2 binding by both directly occluding the binding site and by locking the RBDs into an inactive conformation. Although a multitude of other monoclonal and single-domain antibodies against SARS-CoV-2 Spike have been discovered to date, there are few if any molecules as potent and stable as mNb6-tri [32-42]. Resistance to aerosolization, in particular, offers unprecedented opportunity for patient-friendly nasal and pulmonary administration.

Our discovery of Class II neutralizing nanobodies demonstrates the presence of previously unexplored mechanisms of blocking Spike binding to ACE2. For one Class II nanobody, Nb3, we identified a likely binding site in the Spike S_1 domain external to the RBDs. Previously discovered neutralizing antibodies from convalescent patients bind an epitope in a similar region of Spike [24, 26, 27]. Binding of Nb3 to this epitope may allosterically stabilize RBDs in the down-state, thereby decreasing ACE2 binding. Pairing of Class I and Class II nanobodies in a prophylactic or therapeutic cocktail could thus be a highly advantageous strategy for both potent neutralization and prevention of escape variants. The combined stability, potency, and diverse epitope engagement of our anti-Spike nanobodies therefore provide a unique potential prophylactic and therapeutic strategy to limit the continued toll of the COVID-19 pandemic.

MAIN TEXT FIGURES

Figure 1

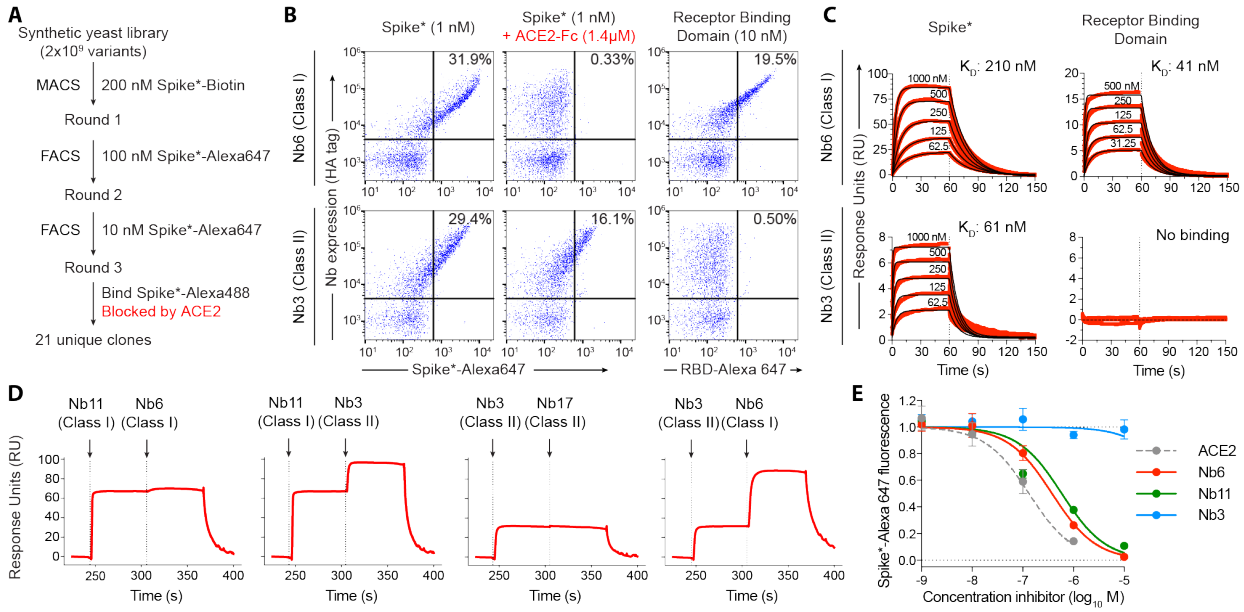

Figure 1. Discovery of two distinct classes of anti-Spike nanobodies. A, Selection strategy for identification of anti-Spike nanobodies that disrupt Spike-ACE2 interactions using magnetic bead selections (MACS) or fluorescence activated cell sorting (FACS). **B,** Flow cytometry of yeast displaying Nb6 (a Class I nanobody) or Nb3 (a Class II nanobody). Nb6 binds Spike*-Alexa 647 and receptor binding domain (RBD-Alexa 647). Nb6 binding to Spike* is completely disrupted by an excess (1.4 μM) of ACE2-Fc. Nb3 binds Spike*, but not the RBD. Nb3 binding to Spike* is partially decreased by ACE2-Fc. **C,** SPR of Nb6 and Nb3 binding to either Spike* or RBD. Red traces are raw data and global kinetic fits are shown in black. Nb3 shows no binding to RBD. **D,** SPR experiments with immobilized Spike* show that Class I and Class II nanobodies can bind Spike* simultaneously. By contrast, two Class I nanobodies or Class II nanobodies do not bind simultaneously. **E,** Nanobody inhibition of 1 nM Spike*-Alexa 647 binding to ACE2 expressing HEK293T cells. n = 3 (ACE2, Nb3) or 5 (Nb6, Nb11) biological replicates. All error bars represent s.e.m.

Figure 2

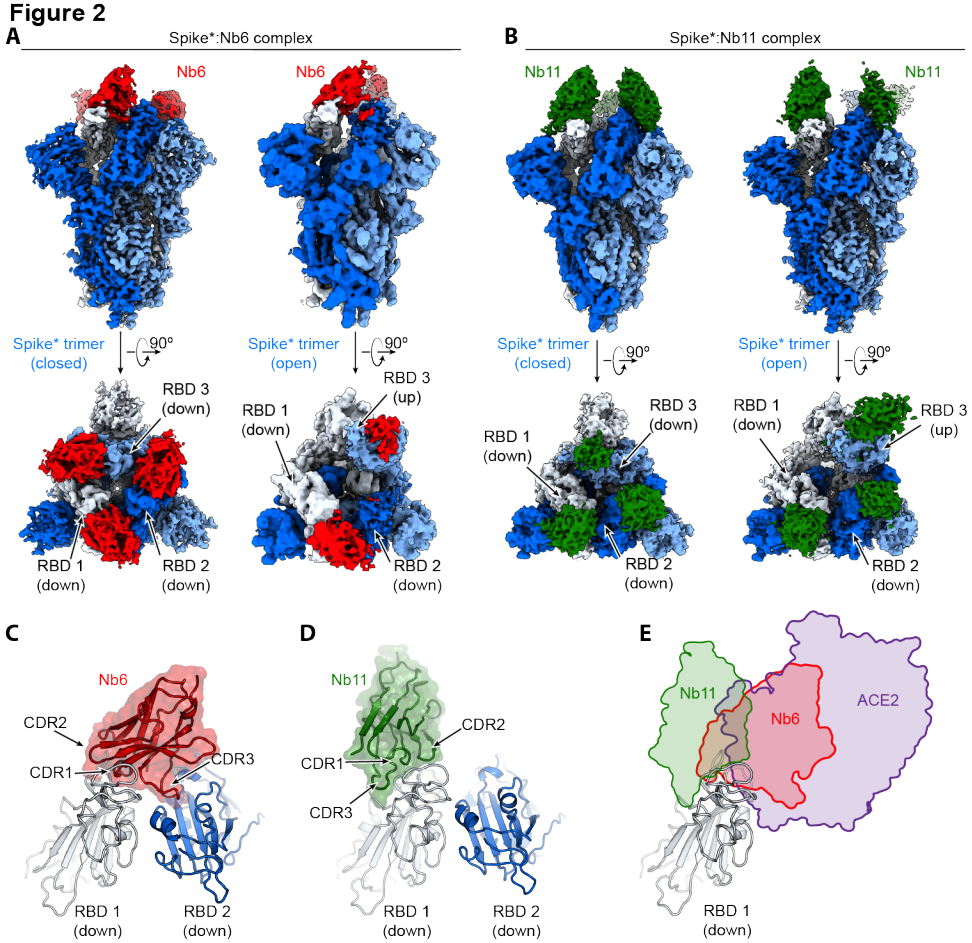

Figure 2. Cryo-EM structures of Nb6 and Nb11 bound to Spike. A, Cryo-EM maps of Spike*-Nb6 complex in either closed (left) or open (right) Spike* conformation. **B,** Cryo-EM maps of Spike*-Nb11 complex in either closed (left) or open (right) Spike* conformation. The top views show receptor binding domain (RBD) up- or down-states. **C,** Nb6 straddles the interface of two down-state RBDs, with CDR3 reaching over to an adjacent RBD. **D,** Nb11 binds a single RBD in the down-state (displayed) or similarly in the up-state. No cross-RBD contacts are made by Nb11 in either RBD up- or down-state. **E,** Comparison of RBD epitopes engaged by ACE2 (purple), Nb6 (red), or Nb11 (green). Both Nb11 and Nb6 directly compete with ACE2 binding.

Figure 3

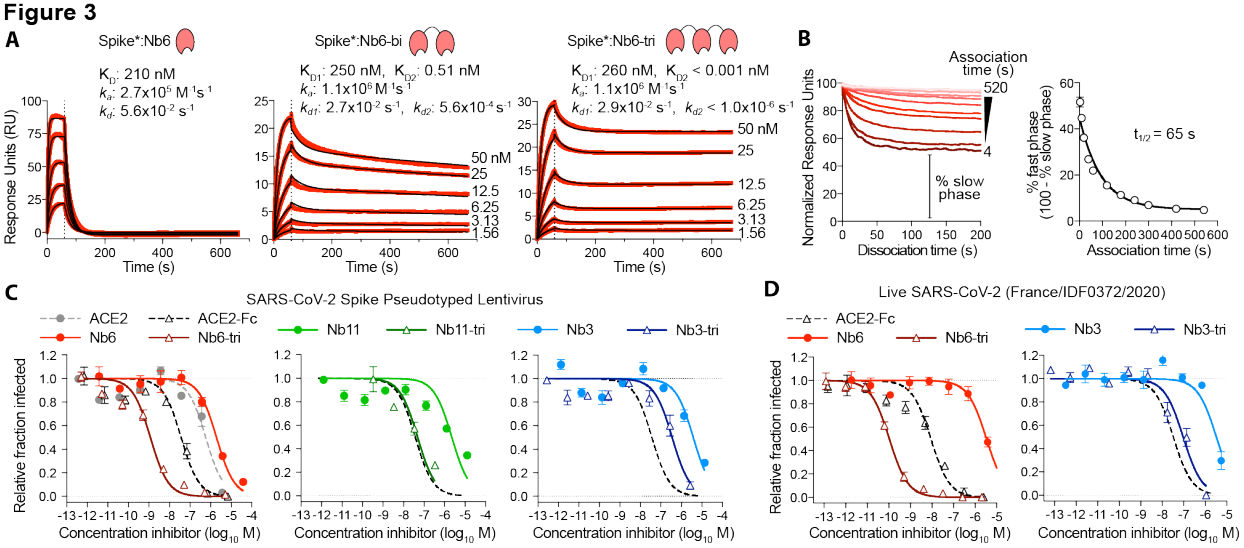

Figure 3. Multivalency improves nanobody affinity and inhibitory efficacy. A, SPR of Nb6 and multivalent variants. Red traces show raw data and black lines show global kinetic fit for Nb6 and independent fits for association and dissociation phases for Nb6-bi and Nb6-tri. **B,** Dissociation phase SPR traces for Nb6-tri after variable association time ranging from 4 to 520 s. Curves were normalized to maximal signal at the beginning of the dissociation phase. Percent fast phase is plotted as a function of association time (right) with a single exponential fit. n = 3 independent biological replicates. **C,** Inhibition of pseudotyped lentivirus infection of ACE2 expressing HEK293T cells. n = 3 biological replicates for all but Nb11-tri (n = 2) **D,** Inhibition of live SARS-CoV-2 virus. Representative biological replicate with n = 3 (right panel) or 4 (left panel) technical replicates per concentration. n = 3 biological replicates for all but Nb3 and Nb3-tri (n = 2). All error bars represent s.e.m.

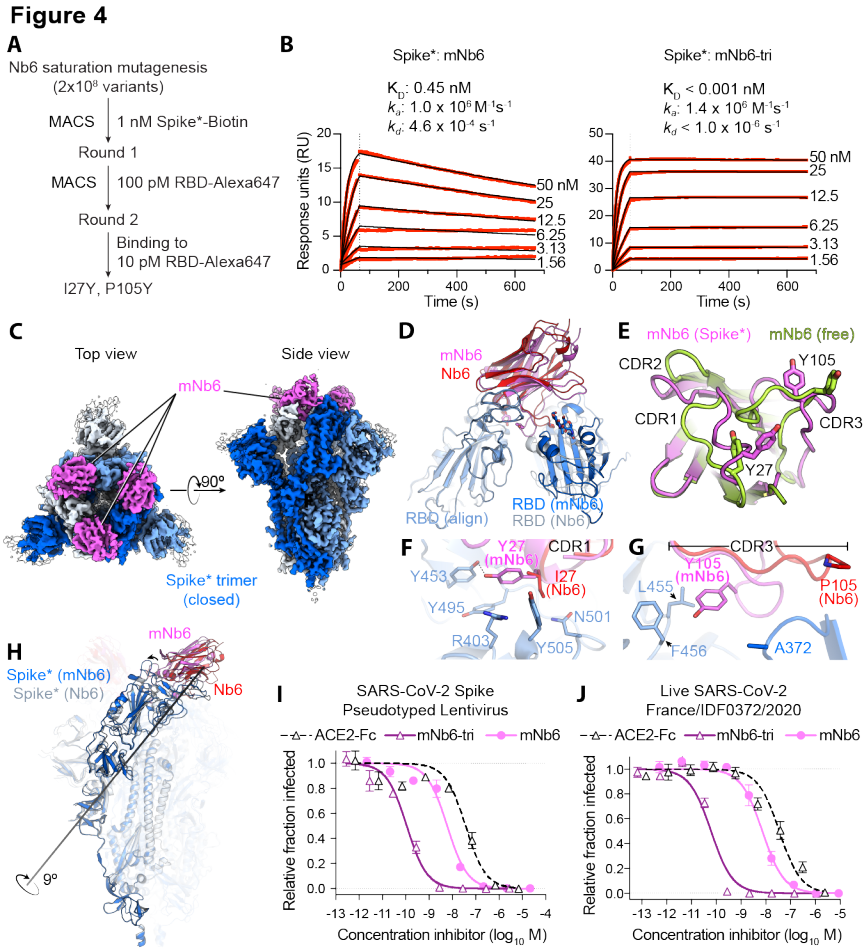

Figure 4. Affinity maturation of Nb6 yields a picomolar SARS-CoV-2 neutralizing molecule. A, A saturation mutagenesis library of Nb6 was subjected to two rounds of selection to identify consensus mutations I27Y and P105Y. **B,** SPR of mNb6 and mNb6-tri binding to immobilized Spike*. Red traces show raw data and black lines show global kinetic fit. No dissociation was observed for mNb6-tri over 10 minutes. **C,** Cryo-EM structure of Spike*-mNb6 complex. **D,** Comparison of receptor binding domain (RBD) engagement by Nb6 and mNb6. One RBD was used to align both structures (RBD align), demonstrating changes in Nb6 and mNb6 position and the adjacent RBD**. E,** Comparison of mNb6 complementarity determining regions in either the cryo-EM structure of the Spike*-mNb6 complex or an X-ray crystal structure of mNb6 alone. **F,** CDR1 of Nb6 and mNb6 binding to the RBD. As compared to I27 in Nb6, Y27 of mNb6 hydrogen bonds to Y453 and optimizes pi-pi and pi-cation interactions with the RBD. **G,** CDR3 of Nb6 and mNb6 binding to the RBD demonstrating a large conformational rearrangement of the entire loop in mNb6. **H,** Comparison of closed Spike* bound to mNb6 and Nb6. Rotational axis for RBD movement is highlighted. **I,** Inhibition of pseudotyped lentivirus

infection of ACE2 expressing HEK293T cells by mNb6 and mNb6-tri. n = 3 biological replicates **J,** mNb6 and mNb6-tri inhibit SARS-CoV-2 infection of VeroE6 cells in a plaque assay. Representative biological replicate with n = 4 technical replicates per concentration. n = 3 biological replicates for all samples. All error bars represent s.e.m.

Figure 5

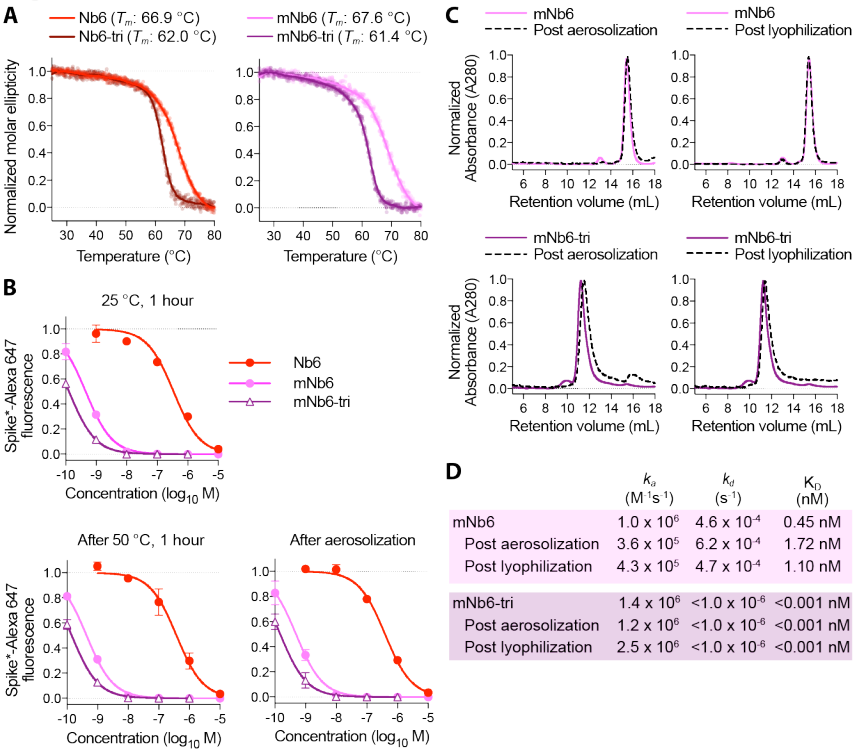

Figure 5. Nb6 and its derivates are robust proteins. A, Thermal denaturation of nanobodies assessed by circular dichroism measurement of molar ellipticity at 204 nm. Apparent melting temperatures (T_m) for each nanobody are indicated. **B,** Nanobody inhibition of 1 nM Spike*-Alexa 647 binding to ACE2 expressing HEK293T cells after incubation at either 25 °C or 50 °C for 1 hour or after aerosolization. **C,** Size exclusion chromatography of nanobodies after lyophilization or aerosolization. **D,** Summary table of SPR kinetics data and affinities for aerosolized or lyophilized mNb6 and mNb6-tri.

Table 1. Anti-Spike nanobody affinity and neutralization potency

Nanobody	Class	Spike* Binding			RBD Binding			Spike* Competition IC_{50} (s.e.m) (M)[a]	SARS-CoV-2 Pseudovirus IC_{50} (s.e.m.) (M)[b]	Live SARS-CoV-2 IC_{50} (s.e.m.) (M)[c]
		k_a ($M^{-1}s^{-1}$)	k_d (s^{-1})	K_D (M)	k_a ($M^{-1}s^{-1}$)	k_d (s^{-1})	K_D (M)			
Nb2	I	$9.0x10^{5}$	$5.3x10^{-1}$	$5.9x10^{-7}$	$1.0x10^{6}$	$9.9x10^{-1}$	$9.7x10^{-7}$	$8.3x10^{-6}$ ($1.7x10^{-6}$)	NP	NP
Nb3	II	$1.8x10^{6}$	$1.1x10^{-1}$	$6.1x10^{-8}$	NB			NC	$3.9x10^{-6}$ ($7.9x10^{-7}$)	$3.0x10^{-6}$ ($3.2x10^{-7}$)
Nb6	I	$2.7x10^{5}$	$5.6x10^{-2}$	$2.1x10^{-7}$	$2.1x10^{6}$	$8.7x10^{-2}$	$4.1x10^{-8}$	$3.7x10^{-7}$ ($4.9x10^{-8}$)	$2.0x10^{-6}$ ($3.5x10^{-7}$)	$3.3x10^{-6}$ ($7.2x10^{-7}$)
Nb8	I	$1.4x10^{5}$	$8.1x10^{-1}$	$5.8x10^{-6}$	$6.6x10^{5}$	$3.3x10^{-1}$	$5.1x10^{-7}$	$4.8x10^{-6}$ ($4.9x10^{-7}$)	NP	NP
Nb11	I	$1.2x10^{6}$	$1.6x10^{-1}$	$1.4x10^{-7}$	$3.2x10^{6}$	$2.4x10^{-1}$	$7.6x10^{-8}$	$5.4x10^{-7}$ ($1.2x10^{-7}$)	$2.4x10^{-6}$ ($5.4x10^{-7}$)	NP
Nb12	I	$1.2x10^{2}$	$2.0x10^{-4}$	$1.6x10^{-6}$	Biphasic	Biphasic	Biphasic	$2.5x10^{-7}$ ($5.5x10^{-8}$)	$1.2x10^{-6}$ ($9.0x10^{-7}$)	NP
Nb15	I	$1.7x10^{5}$	$2.3x10^{-1}$	$1.3x10^{-6}$	$6.0x10^{5}$	$2.2x10^{-1}$	$3.6x10^{-7}$	$2.2x10^{-6}$ ($2.5x10^{-7}$)	$6.7x10^{-6}$ ($3.6x10^{-6}$)	NP
Nb16	I	$1.1x10^{5}$	$1.3x10^{-1}$	$1.3x10^{-6}$	NP			$9.5x10^{-7}$ ($1.1x10^{-7}$)	NP	NP
Nb17	II	$7.3x10^{5}$	$2.0x10^{-1}$	$2.7x10^{-7}$	NB			NC	$7.6x10^{-6}$ ($1.0x10^{-6}$)	NP
Nb18	II	$1.4x10^{5}$	$6.4x10^{-3}$	$4.5x10^{-8}$	NB			$5.2x10^{-5}$ ($1.5x10^{-5}$)	NP	NP
Nb19	I	$2.4x10^{4}$	$1.1x10^{-1}$	$4.5x10^{-6}$	$1.0x10^{5}$	$8.9x10^{-2}$	$8.8x10^{-7}$	$4.1x10^{-6}$ ($4.9x10^{-7}$)	$2.4x10^{-5}$ ($7.7x10^{-6}$)	NP
Nb24	I	$9.3x10^{5}$	$2.7x10^{-1}$	$2.9x10^{-7}$	$2.4x10^{6}$	$3.5x10^{-1}$	$1.5x10^{-7}$	$7.5x10^{-7}$ ($1.0x10^{-7}$)	NP	NP
ACE2	N/A	$2.7x10^{5}$	$1.2x10^{-2}$	$4.4x10^{-8}$	NP	NP	NP	$1.7x10^{-7}$ ($6.6x10^{-8}$)	$6.2x10^{-7}$ ($1.7x10^{-7}$)	NP
mNb6	I	$1.0x10^{6}$	$4.5x10^{-4}$	$4.5x10^{-10}$	$1.1x10^{6}$	$6.4x10^{-4}$	$5.6x10^{-10}$	$1.3x10^{-9}$ ($4.1x10^{-10}$)	$6.3x10^{-9}$ ($1.6x10^{-9}$)	$1.2x10^{-8}$ ($2.5x10^{-9}$)
Nb3-bi	II	NP	NP	NP	NP	NP	NP	NP	$3.6x10^{-7}$ ($1.5x10^{-7}$)	$1.8x10^{-7}$ ($1.2x10^{-8}$)
Nb3-tri	II	Biphasic	Biphasic	Biphasic	NP	NP	NP	$4.1x10^{-8}$ ($1.6x10^{-8}$)	$4.0x10^{-7}$ ($1.6x10^{-7}$)	$1.4x10^{-7}$ ($4.9x10^{-8}$)
Nb6-bi	I	Biphasic	Biphasic	Biphasic	NP	NP	NP	NP	$6.3x10^{-8}$ ($1.5x10^{-8}$)	NP
Nb6-tri	I	Biphasic	Biphasic	Biphasic	NP	NP	NP	$1.5x10^{-9}$ ($5.2x10^{-10}$)	$1.2x10^{-9}$ ($2.5x10^{-10}$)	$1.6x10^{-10}$ ($2.6x10^{-11}$)
Nb11-tri	I	Biphasic	Biphasic	Biphasic	NP	NP	NP	NP	$5.1x10^{-8}$ ($1.6x10^{-8}$)	NP
ACE2-Fc	N/A	NP	NP	NP	NP	NP	NP	$5.3x10^{-9}$ ($2.5x10^{-9}$)	$4.0x10^{-8}$ ($8.8x10^{-9}$)	$2.6x10^{-8}$ ($8.5x10^{-9}$)
mNb6-tri	I	$1.4x10^{6}$	$<1.0x10^{-6}$	$<1.0x10^{-12}$	NP	NP	NP	$4.0x10^{-10}$ ($1.4x10^{-10}$)	$1.2x10^{-10}$ ($2.8x10^{-11}$)	$5.4x10^{-11}$ ($1.0x10^{-11}$)

[a]Average values from n = 5 biological replicates for Nb6, Nb11, Nb15, Nb19 are presented, all others were tested with n = 3 biological replicates.

[b]Average values from n = 2 biological replicates for Nb12, Nb17, and Nb11-tri are presented, all others were tested with n = 3 biological replicates.

[c]Average values from n = 2 biological replicates for Nb3, Nb3-bi, and Nb3-tri. n = 3 biological replicates for all others.

NB – no binding

NC – no competition

NP – not performed

Supplementary Figures

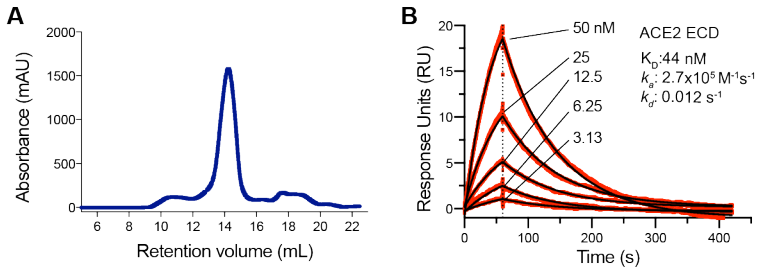

Supplementary Fig. 1. Validation of purified Spike*. A, Size exclusion chromatogram of purified Spike* from ExpiCHO cells. **B,** SPR of immobilized Spike* binding to monomeric ACE2 extracellular domain (ECD).

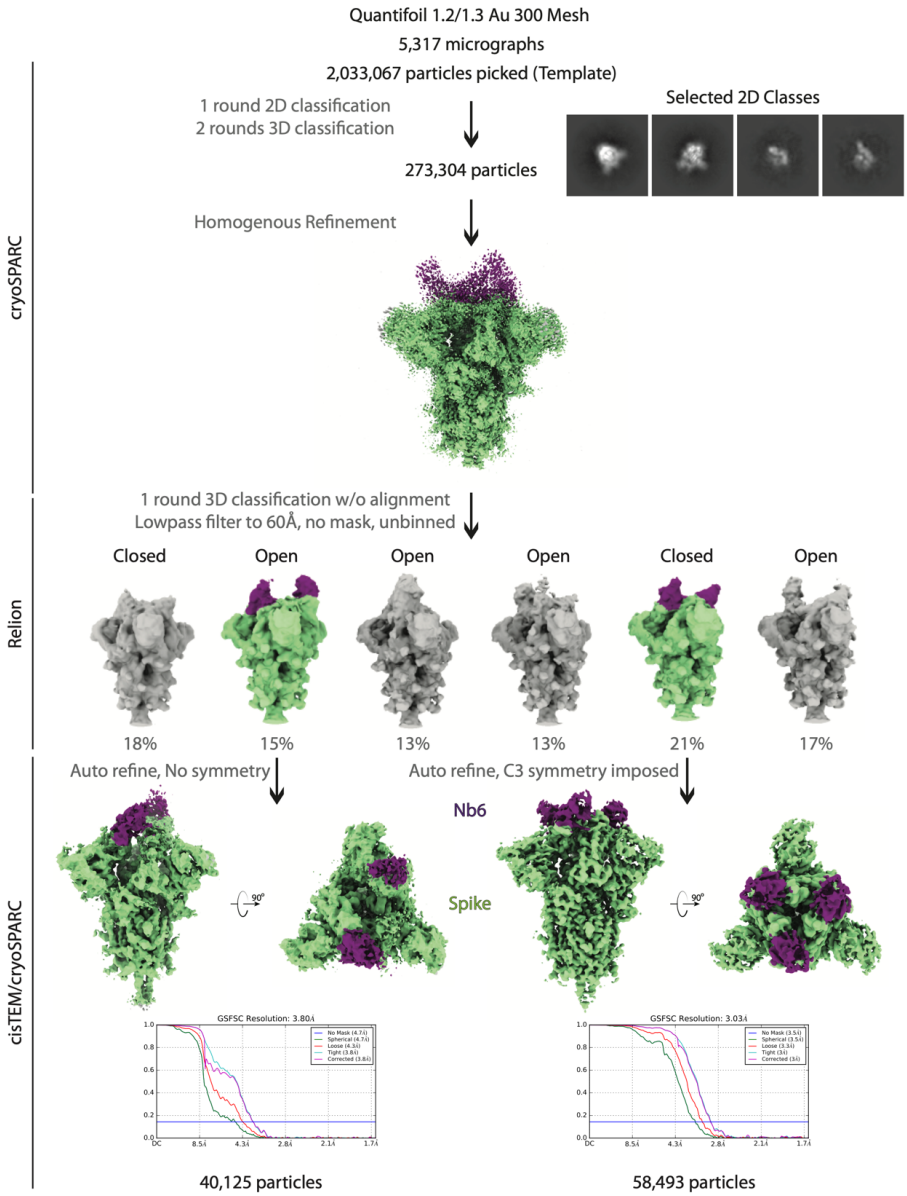

Supplementary Fig. 2. Cryo-EM workflow for Nb6

A flowchart representation of the classification workflow for Spike*-Nb6 complexes yielding open and closed Spike* conformations. From top to bottom, particles were template picked with a set of 20 Å low-pass filtered 2D backprojections of apo-Spike* in the closed conformation. Extracted particles in 2D classes suggestive of various Spike* views were subject to a round of heterogenous refinement in cryoSPARC with two naïve classes generated from a truncated *Ab initio* job, and a 20 Å low-pass filtered volume of apo-Spike* in the closed conformation. Particles in the Spike* 3D class were subject to 25 iterations of 3D classification into 6 classes without alignment in RELION, using the same input volume from cryoSPARC 3D classification,

low pass filtered to 60 Å, T = 8. Particles in classes representing the open and closed Spike* conformations were imported into cisTEM for automatic refinement. Half maps from refinement were imported into cryoSPARC for local resolution estimation as shown in Supplementary Fig. 4.

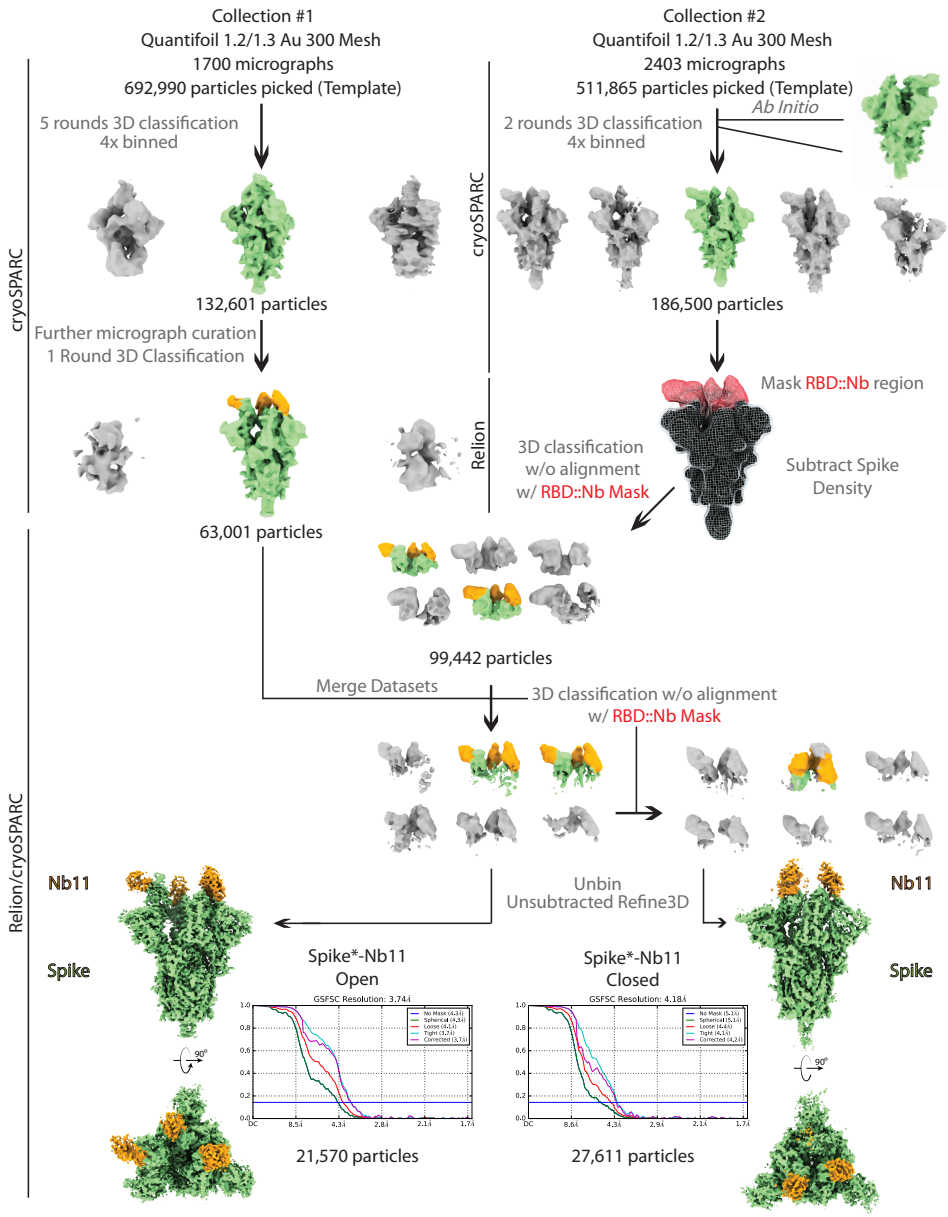

Supplementary Fig. 3. Cryo-EM workflow for Nb11

A flowchart representation of the classification workflow for Spike*-Nb11 complexes yielding open and closed Spike* conformations. From top to bottom, particles were template picked from two separate collections with a set of 20 Å low-pass filtered 2D backprojections of apo-Spike* in the closed conformation. Extracted particles were Fourier cropped to 128 pixels prior to extensive heterogenous refinement in cryoSPARC, using a 20 Å low-pass filtered volume of apo-Spike* in the closed conformation and additional naïve classes for removal of non-Spike* particles. After cryoSPARC micrograph curation and heterogenous refinement, Spike* density corresponding to all regions outside of the ACE2 RBD::Nanobody interface were subtracted. A

mask around the ACE2 RBD::Nanobody interface was generated, and used for multiple rounds of 3D classification without alignment in RELION. Particles in classes representing open and closed Spike* conformations were selected, unsubtracted and unbinned prior to refinement in RELION. Half maps from refinement were imported into cryoSPARC for local resolution estimation as shown in Supplementary Fig. 4.

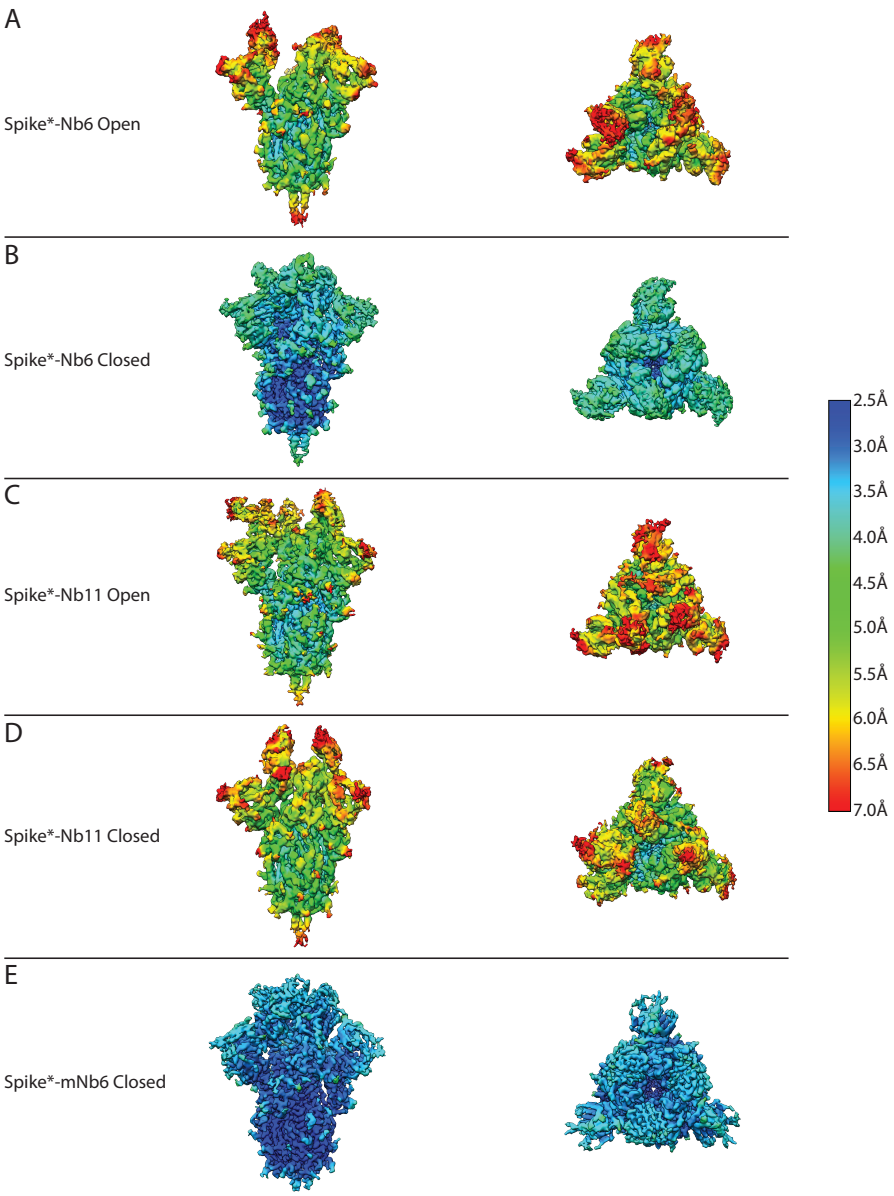

444

445 **Supplementary Fig. 4. Local resolution of cryo-EM maps**

446 Local resolution estimates of Spike* complexes with A-B) Nb6, C-D) Nb11, and E) mNb6 as
447 generated in cryoSPARC. All maps (except mNb6) are shown with the same enclosed volume.
448 All maps are colored on the same scale, as indicated.

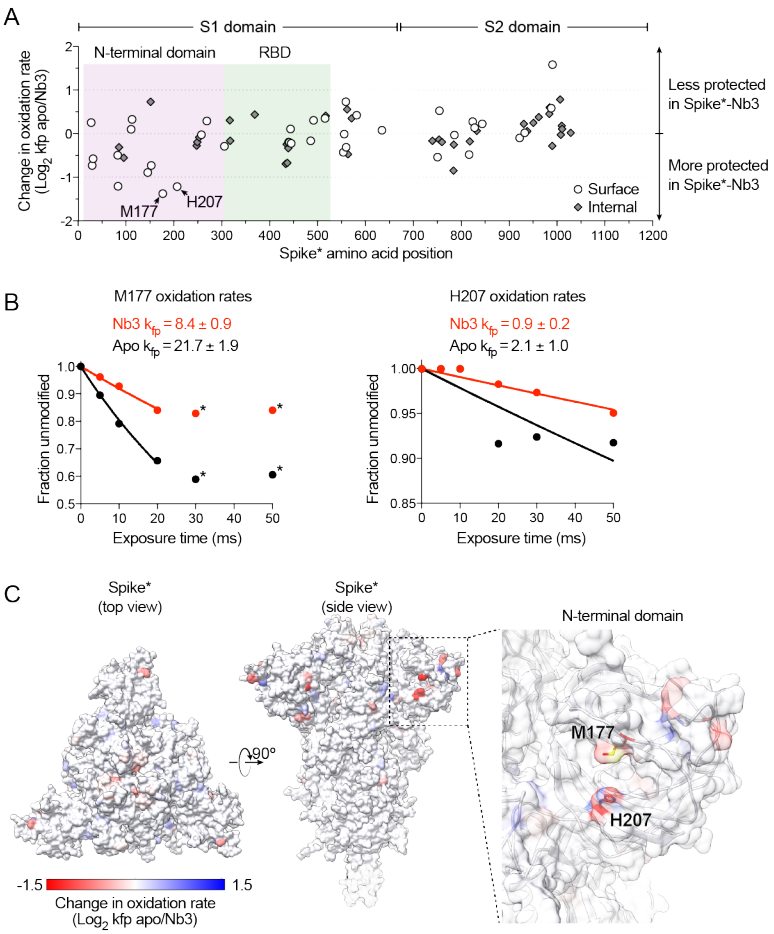

Supplementary Fig. 5. Radiolytic hydroxyl radical footprinting of Spike*.

A, Change in oxidation rate between Spike* and Nb3-Spike* complexes at all residues. A cluster of highly protected residues in the Spike*-Nb3 complex is observed in the N-terminal domain. **B,** Oxidation rate plots of the two (M177, H207) most heavily protected residues upon Nb3 binding to Spike*. Data points labeled with an asterisk are excluded from rate calculations as these values fall outside of the first order reaction, likely due to extensive oxidation-mediated damage. **C,** Change in oxidation rate mapped onto Spike in the all RBD down conformation.

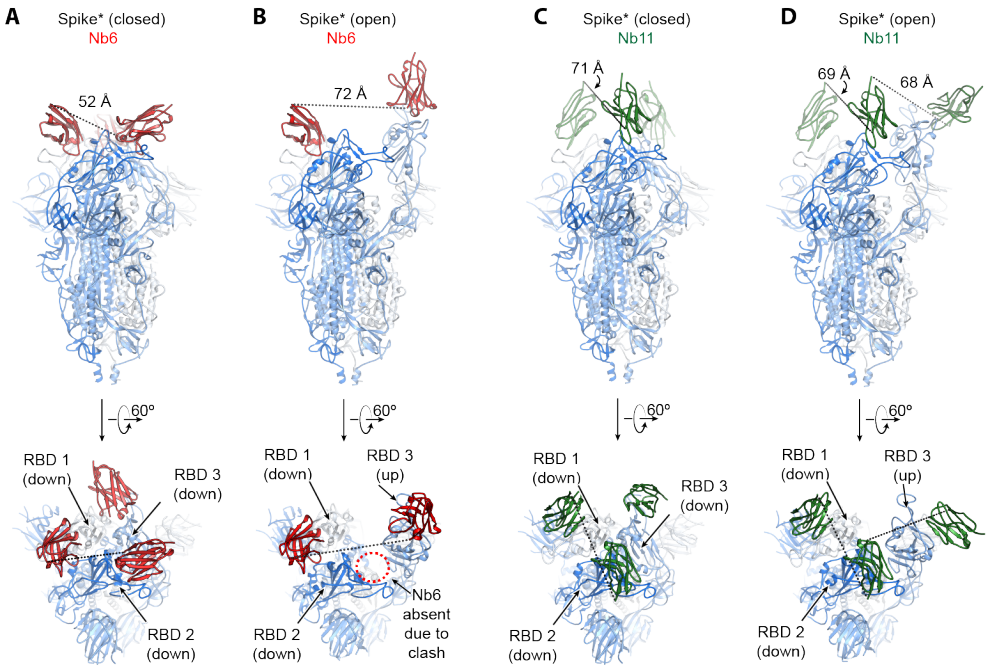

Supplementary Fig. 6. Modeling of distances for multimeric nanobody design. A, Model of Spike*:Nb6 complex in the closed state. The minimal distance between adjacent Nb6 N- and C-termini is 52 Å (dashed line). **B,** Model of Spike*:Nb6 complex in the open state with Nb6 docked into the cryo-EM density for up-state RBD. Minimal distance between N- and C-termini of both nanobodies is 72 Å**.** Nb6 cannot bind RBD2 in open Spike*, as this would sterically clash with RBD3. **C,** Model of Spike*:Nb11 complex in the closed state. The minimal distance between adjacent Nb6 N- and C-termini is 71 Å (dashed line). **D,** Model of Spike*:Nb11 complex in the open state. The minimal distance between adjacent Nb6 N- and C-termini is 68 Å between Nb11 bound to RBD2 in the down-state and RBD3 in the up-state. For B, the model of Nb6 from A was docked into the cryo-EM map to enable modeling of distance between N- and C-termini. For C and D, a generic nanobody was docked into cryo-EM maps to model the distance between N- and C-termini.

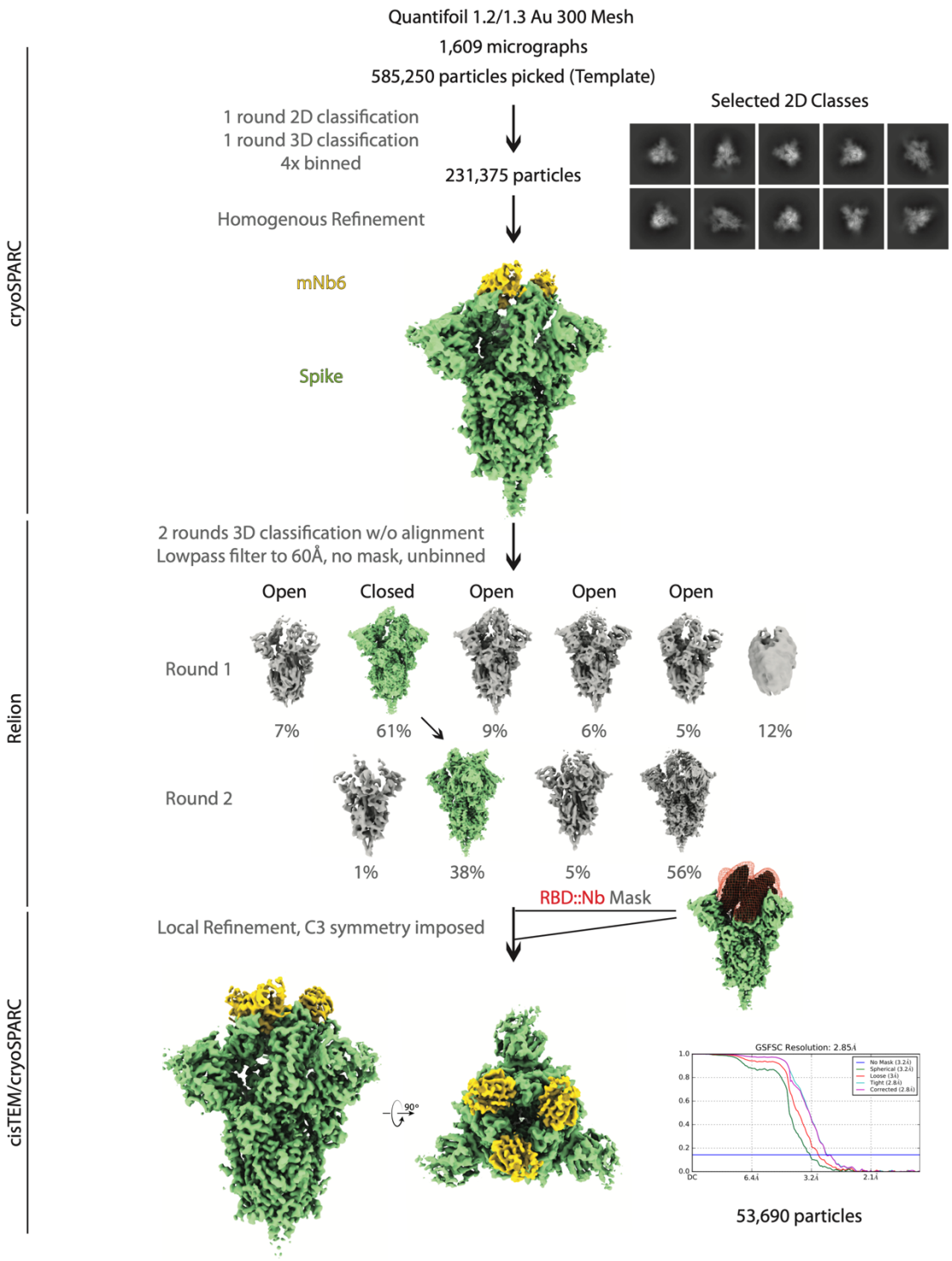

Supplementary Fig. 7. CryoEM workflow for mNb6

A flowchart representation of the classification workflow for the Spike*-mNb6 complex yielding a closed Spike* conformation. From top to bottom, particles were template picked from two separate collections with a set of 20Å low-pass filtered 2D backprojections of apo-Spike* in the

closed conformation. Extracted particles were Fourier cropped to 96 pixels prior to 2D classification. Particles in Spike* 2D classes were selected for a round of heterogeneous refinement in cryoSPARC using a 20 Å low-pass filtered volume of apo-Spike* in the closed conformation and additional naïve classes for removal of non-Spike* particles. In RELION, particles in the Spike* 3D class were subject to two rounds of 3D classification without alignment into 6 classes using the same input volume from cryoSPARC 3D classification, low pass filtered to 60 Å, T = 8. Unbinned particles in the Spike*-closed conformation were exported into cisTEM for automatic refinement, followed by local refinement using a mask around the ACE2 RBD::Nanobody interface. Half maps from refinement were imported into cryoSPARC for local resolution estimation as shown in Supplementary Fig. 4.

Supplementary Table 1. CryoEM datasets

Sample:	Spike*-Nb6		Spike*-Nb11		Spike*-mNb6
Spike* conformation:	Open	Closed	Open	Closed	Closed
EMDB:	XXXX	XXXX	XXXX	XXXX	XXXX
PDB:		XXXX			XXXX
Data collection and processing					
Microscope/Detector	Titan Krios/Gatan K3 with Gatan Bioquantum Energy Filter				
Imaging software and collection	SerialEM, 3x3 image shift				
Magnification	105,000				
Voltage (kV)	300				
Electron exposure (e–/Å^2)	66				
Dose rate (e–/pix/sec)	8				
Frame exposure (e–/Å^2)	0.55				
Defocus range (μm)	-0.8 to -2.0				
Pixel size (Å)	0.834 (physical)				
Micrographs	5,317		4,103		1,609
Reconstruction					
Autopicked particles (template-based in cryosparc)	2,033,067		1,204,855		585,250
Particles in final refinement	40,125 (cisTEM)	58,493 (cisTEM)	21,570 (cisTEM)	27,611 (RELION)	53,690 (cisTEM)
Symmetry imposed	C1	C3	C1	C1	C3
Map sharpening *B* factor (Å^2)		-90			-140
Map resolution, global FSC (Å)					
FSC 0.5, unmasked/masked	7.8/4.6	4.1/3.4	7.0/4.4	7.6/5.3	3.9/3.3
FSC 0.143, unmasked/masked	4.7/3.8	3.5/3.0	4.3/3.7	5.1/4.2	3.2/2.9
Refinement					
Initial model used (PDB code)		6VXX, 3P0G			6VXX, 3P0G
Model resolution (Å)					
FSC 0.5, unmasked/masked		3.5/3.1			3.2/2.9
Model composition					
Non-hydrogen atoms		26904			27015
Protein residues		3360			3360
B factors (Å^2)					
Protein		97.0			57.5
Ligand		107.4			85.7
R.m.s. deviations					
Bond lengths (Å)		0.014			0.007
Bond angles (°)		1.379			1.027
Validation					
MolProbity score		1.99			1.71
Clashscore		12.70			6.46
Poor rotamers (%)		0.45			0.41
EMRinger score		2.98			4.01
CaBLAM score		3.11			2.95
Ramachandran plot					
Favored (%)		94.49			94.92
Allowed (%)		5.51			5.08
Disallowed (%)		0			0

Supplementary Table 2. X-ray data collection and refinement statistics

	mNb6 (PDB XXXX)
Data collection	
Space group	$P2_1$
Cell dimensions	
a, *b*, *c* (Å)	44.56, 71.25, 46.43
α, β, γ (°)	90.0, 114.93, 90.0
Molecules in asymmetric unit	2
Resolution (Å)	71.25 - 2.05 (2.09 - 2.05)[a]
R_{sym} or R_{merge}	0.13 (0.94)[b]
$I / \sigma I$	7.2 (0.9)
Completeness (%)	97.8 (96.6)
Redundancy	6.4 (5.7)
CC (1/2) (%)	99.8 (64.4)
Refinement	
Resolution (Å)	71.25 – 2.05
No. reflections	104195
R_{work} / R_{free} (%)	21.16 / 24.75
No. atoms	
Protein	1798
Ligand/ion	21
Water	131
B-factors	
Protein	33.1
Ligand/ion	76.1
Water	42.2
R.m.s. deviations	
Bond lengths (Å)	0.07
Bond angles (°)	0.826
Ramachandran plot	
Allowed (%)	99.06
Generous (%)	0.94
Disallowed (%)	0

[a] Values in parentheses correspond to the highest resolution shell.

[b] $R_{merge} = \Sigma|I - \langle I \rangle|/\Sigma I$

[c] $R_{work} = \Sigma|F_O - F_C|/\Sigma F_O$

[d] $R_{free} = \Sigma|F_O - F_C|/\Sigma F_O$, calculated using a random set containing 5% reflections that were not included throughout structure refinement.

Supplementary Table 3. Nanobody expression plasmids

Plasmid	Nanobody	Plasmid backbone	Resistance Marker
pPW3544	Nb2	pet-26b(+)	kanamycin
pPW3545	Nb3	pet-26b(+)	kanamycin
pPW3546	Nb6	pet-26b(+)	kanamycin
pPW3547	Nb8	pet-26b(+)	kanamycin
pPW3548	Nb11	pet-26b(+)	kanamycin
pPW3549	Nb12	pet-26b(+)	kanamycin
pPW3550	Nb15	pet-26b(+)	kanamycin
pPW3551	Nb16	pet-26b(+)	kanamycin
pPW3552	Nb17	pet-26b(+)	kanamycin
pPW3553	Nb18	pet-26b(+)	kanamycin
pPW3554	Nb19	pet-26b(+)	kanamycin
pPW3555	Nb24	pet-26b(+)	kanamycin
pPW3557	Trivalent Nb6, 20AA length GS linker	pet-26b(+)	kanamycin
pPW3558	Trivalent Nb3, 15AA length GS linker	pet-26b(+)	kanamycin
pPW3559	Trivalent Nb11, 15AA length GS linker	pet-26b(+)	kanamycin
pPW3560	Bivalent Nb3, 15AA length GS linker	pet-26b(+)	kanamycin
pPW3561	Bivalent Nb6, 15AA length GS linker	pet-26b(+)	kanamycin
pPW3563	Trivalent mNb6, 20AA length GS linker	pet-26b(+)	kanamycin
pPW3564	mNb6	pet-26b(+)	kanamycin

METHODS

Expression and purification of SARS-CoV-2 Spike, RBD, and ACE2.

We used a previously described construct to express and purify the pre-fusion SARS-CoV-2 Spike ectodomain (Spike*) [15]. ExpiCHO or Expi293T cells (ThermoFisher) were transfected with the Spike* construct per the manufacturer's instructions for the MaxTiter protocol and harvested between 3-9 days after transfection. Clarified cell culture supernatant was loaded onto Ni-Excel beads (Cytiva) followed by extensive washes in 20 mM HEPES pH 8.0, 200 mM sodium chloride, and 10 mM imidazole and elution in the same buffer supplemented with 500 mM imidazole. Spike* was concentrated using a 100 kDa MWCO spin concentrator (Millipore) and further purified by size exclusion chromatography over a Superose 6 Increase 10/300 column (GE Healthcare) in 20 mM HEPES pH 8.0 and 200 mM sodium chloride. All purification steps were performed at room temperature. The resulting fractions for trimeric Spike* were pooled and either used directly for cryo-EM studies or concentrated and flash frozen in liquid nitrogen with 15% glycerol for other biochemical studies.

We used a previously described construct to express and purify the SARS-CoV-2 Receptor binding domain (RBD) [43]. Expi293T cells (ThermoFisher) were transfected with the RBD construct per the manufacturer's instructions and harvested between 3-6 days after transfection. Clarified cell culture supernatant was loaded onto Ni-Excel beads (Cytiva) or a His-Trap Excel column (GE Healthcare) followed by washes in 20 mM HEPES pH 8.0, 200 mM sodium chloride, and 10 mM imidazole and elution using the same buffer supplemented with 500 mM imidazole. RBD was concentrated using a 30 kDa MWCO spin concentrator (Millipore) and further purified by size exclusion chromatography over a Superdex 200 Increase 10/300 GL column (GE Healthcare) in 20 mM HEPES pH 8.0 and 200 mM sodium chloride. The resulting fractions were pooled, concentrated, and flash frozen in liquid nitrogen with 10% glycerol.

For biochemical and yeast display experiments, Spike* and RBD were labeled with freshly prepared stocks of Alexa 647-NHS, Alexa 488-NHS, or Biotin-NHS (ThermoFisher) with a 5-fold stoichiometry for 1 hour at room temperature followed by quenching of NHS with 10 mM Tris pH 8.0 for 60 minutes. Labeled proteins were further purified by size exclusion chromatography, concentrated using a spin concentrator (Millipore), and flash frozen in liquid nitrogen with 10-15% glycerol.

We used an ACE2-ECD (18-614) Fc fusion expression plasmid to express and purify Fc tagged ACE2-ECD [44]. Expi293T cells (ThermoFisher) were transfected with the ACE2-Fc construct per the manufacturer's instructions and harvested between 5-7 days after transfection. Clarified cell culture supernatant was loaded onto a MabSelect Pure 1 mL Column (GE Healthcare). Column was washed with Buffer A (20 mM HEPES pH 7.5, 150 mM NaCl) and protein was eluted with Buffer B (100 mM Sodium Citrate pH 3.0, 150 mM NaCl) into a deep well block containing 1 M HEPES pH 7.5 to neutralize the acidic elution. ACE2-Fc was concentrated using a 30 kDa MWCO spin concentrator (Millipore) and further purified by size exclusion chromatography over a Superdex 200 Increase 10/300 GL column (GE Healthcare) in SEC Buffer (20 mM HEPES pH 7.5, 150 mM NaCl, 5% v/v Glycerol). The resulting fractions were pooled, concentrated, and flash frozen in liquid nitrogen. To obtain monomeric ACE2, 1:50 (w/w) His-tagged TEV protease was added to ACE2-Fc and incubated at 4 °C overnight. This mixture was then purified by size exclusion chromatography in SEC Buffer. Monomeric ACE2 fractions were pooled and washed with His-resin (1 mL of 50% slurry) to remove excess TEV. The resulting supernatant was pooled, concentrated, and flash frozen in liquid nitrogen.

Identification of anti SARS-CoV2 Spike nanobodies

To identify nanobodies against the SARS-CoV-2 Spike ECD, we used a yeast surface displayed library of synthetic nanobody sequences that recapitulate amino acid position specific-variation in natural llama immunological repertoires. This library encodes a diversity of $>2x10^9$ variants, and uses a synthetic stalk sequence for nanobody display, as described previously in a modified vector encoding nourseothricin (NTC) resistance [45]. For the first round of selection, $2x10^{10}$ yeast induced in YPG (Yeast Extract-Peptone-Galactose) supplemented with NTC were washed repeatedly in selection buffer (20 mM HEPES, pH 7.5, 150 mM sodium chloride, 0.1% (w/v) low biotin bovine serum albumin, BSA) and finally resuspended in 10 mL of selection buffer containing 200 nM biotinylated-Spike*. Yeast were incubated for 30 minutes at 25 °C, then washed repeatedly in cold selection buffer, and finally resuspended in 10 mL of cold selection buffer containing 200 µL of Miltenyi anti-Streptavidin microbeads. After 30 minutes of incubation at 4 °C, yeast were again washed with cold selection buffer. Spike* binding yeast were captured on a Miltenyi MACS LS column and recovered in YPD (Yeast Extract-Peptone-Dextrose) medium supplemented with NTC.

For round 2, $4x10^8$ induced yeast from Round 1 were incubated with 100 nM Spike* labeled with Alexa647 in 1 mL of selection buffer for 1 hr at 25 °C. After extensive washes with cold selection

buffer, Spike* binding yeast were isolated by fluorescence activated cell sorting (FACS) on a Sony SH800 instrument. A similar approach was used for round 3, with substitution of 10 nM Spike* labeled with Alexa647. Post round 3 yeast were plated on YPD+NTC solid media and 768 individual colonies were induced with YPG+NTC media in 2 mL deep well plates. Each individual clone was tested for binding to 4 nM Spike*-Alexa488 by flow cytometry on a Beckman Coulter Cytoflex. To identify nanobodies that disrupt Spike-ACE2 interactions, Spike* binding was repeated in the presence of 0.5-1 μM ACE2-Fc. Out of 768 clones, we identified 21 that strongly bind Spike* and are competitive with ACE2 (Supplementary Table 3).

Expression and purification of nanobodies

Nanobody sequences were cloned into the pET26-b(+) expression vector using In-Fusion HD cloning (Takara Bio), transformed into BL21(DE3) *E. coli*, grown in Terrific Broth at 37 °C until OD 0.7-0.8, followed by gene induction using 1 mM IPTG for 18-22 hours at 25°C. *E. Coli* were harvested and resuspended in SET Buffer (200 mM Tris, pH 8.0, 500 mM sucrose, 0.5 mM EDTA, 1X cOmplete protease inhibitor (Roche)) for 30 minutes at 25 °C before a 45 minute osmotic shock with a two-fold volume addition of water. NaCl, MgCl2, and imidazole were added to the lysate to 150 mM, 2 mM, and 40 mM respectively before centrifugation at 17-20,000xg for 15 minutes to separate cell debris from the periplasmic fraction. For every liter of bacterial culture, the periplasmic fraction was then incubated with 4 mL of 50% HisPur Ni-NTA resin (Thermo Scientific) which had been equilibrated in Nickel Wash Buffer (20 mM HEPES, pH 7.5, 150 mM NaCl, 40 mM imidazole). This mixture was incubated for 1 hr with rotation at RT before centrifugation at 50xg to collect the resin. The resin was then washed with 5 volumes of Nickel Wash buffer 3 times, each time using centrifugation to remove excess wash buffer. Bound proteins were then eluted using three washes with Elution Buffer (20 mM HEPES, pH 7.5, 150 mM NaCl, 500 mM imidazole). The eluted protein was concentrated using a 3.5 kDa MWCO centrifugal filter unit (Amicon) before injection onto a Superdex 200 Increase 10/300 GL column equilibrated with 20 mM HEPES, pH 7.5, 150 mM NaCl. Nanobody constructs were concentrated again using a 3.5k MWCO centrifugal filter unit, and flash frozen in liquid nitrogen.

Affinity determination by surface plasmon resonance

Nanobody (Nb) affinity determination experiments were performed on Biacore T200 and 8K instruments (Cytiva Life Sciences) by capturing the StreptagII-tagged Spike* at 10 μg/mL on a StreptactinXT-immobilized (Iba Life Sciences) CM5 Series S sensor chip (Cytiva Life Sciences) to achieve maximum response (Rmax) of approximately 30 response units (RUs) upon

nanobody binding. 2-fold serial dilutions of purified nanobody from 1 μM to 31.25 nM (for monovalent constructs) or from 50 nM to 1.56 nM (for affinity matured and multimeric constructs) were flowed over the captured Spike* surface at 30 μL/minute for 60 seconds followed by 600 seconds of dissociation flow. Following each cycle, the chip surface was regenerated with 3 M guanidine hydrochloride.

Separately, biotinylated SARS-CoV-2 RBD at 8 μg/mL was loaded onto a preconditioned Series S Sensor Chip CAP chip (Cytiva Life Sciences) to achieve an Rmax of approximately 60 RUs upon nanobody binding. 2-fold serial dilutions in the same running buffer and sample series (parent or affinity matured clone) as the Spike* runs were flowed over the RBD surface at 30 μL/minute for 60 seconds followed by 600 seconds of dissociation flow. Chip surface regeneration was performed with a guanidine hydrochloride/sodium hydroxide solution.

The resulting sensorgrams for all monovalent clones were fit to a 1:1 Langmuir binding model using the Biacore Insight Evaluation Software (Cytiva Life Sciences) or the association/dissociation model in GraphPad Prism 8.0. For determination of kinetic parameters for Nb6-bi and Nb6-tri binding, the dissociation phase was fit to a biexponential decay constrained to two dissociation rate constants shared between each concentration. The association phase was fit separately using an association kinetics model simultaneously fitting the association rate constant for each concentration.

For nanobody competition experiments, Spike* was loaded onto a StreptactinXT-immobilized CM5 sensor chip as previously described. As in the kinetics experiments, the primary nanobody was flowed over the captured Spike* surface for 60 seconds at 30 μL/minute to achieve saturation. Immediately following this, a second injection of a mixture of primary and variable nanobody at the same concentration as in the primary injection was performed.

ACE2 cellular surface binding competition assays

A dilution series of nanobody was generated in PBE (PBS + 0.5% (w/v) BSA + 2 mM EDTA and mixed with Spike*-Alexa647 or RBD-Alexa647. ACE2 expressing HEK293T cells were dissociated with TrypLE Express (ThermoFisher) and resuspended in PBE [20]. The cells were mixed with the Spike*-nanobody solution and incubated for 45 minutes, washed in PBE, and then resuspended in PBE. Cell surface Alexa647 fluorescence intensity was assessed on an Attune Flow Cytometer (ThermoFisher).

Affinity maturation of Nb6

A site saturation mutagenesis library of Nb6 was generated by assembly PCR of overlapping oligonucleotides encoding the Nb6 sequence. Individual oligos for each position in CDR1, CDR2, and CDR3 were designed with the degenerate “NNK” codon. The assembled gene product was amplified with oligonucleotides with overlapping ends to enable homologous recombination with the yeast surface display vector as previously described and purified with standard silica-based chromatography [45]. The resulting insert DNA was transformed into *Saccharomyces cerevisiae* strain BJ5465 along with the yeast display vector pYDS2.0 to generate a library of $2x10^8$ transformants. After induction in YPD+NTC medium at 20 °C for 2 days, $2x10^9$ yeast were washed in selection buffer (20 mM HEPES, pH 8.0, 150 mM sodium chloride, 0.1% (w/v) low biotin BSA) and incubated with 1 nM biotin-Spike* for 1 hour at 25 °C. Yeast were subsequently washed in selection buffer, resuspended in 1 mL selection buffer, and incubated with 10 µL streptavidin microbeads (Miltenyi) for 15 min. at 4 °C. Yeast were washed again with cold selection buffer and Spike*-binding yeast were isolated by magnetic separation using an LS column (Miltenyi). Recovered yeast were grown in YPD+NTC at 37 °C and induced in YPG+NTC at 20 °C. A second round of selection was performed as above, substituting 100 pM RBD-Alexa647 as the antigen. Yeast displaying high affinity clones were selected by magnetic separation using Anti-Cy5 microbeads (Miltenyi) and an LS column. Analysis of the library after the second round of selection revealed a population of clones with clear binding of 10 pM RBD-Alexa647. Therefore, 96 individual clones were screened for binding to 10 pM RBD-Alexa647 by flow cytometry. Sequence analysis of eight clones that showed robust binding to 10 pM RBD-Alexa647 revealed two consensus mutations, I27Y and P105Y, which were used to generate the affinity matured clone mNb6.

Structures of Spike-nanobody complexes by cryo-EM

Sample preparation and microscopy

To prepare Spike*-nanobody complexes, each nanobody was incubated on ice at a 3-fold molar excess to Spike* at 2.5 µM for 10 minutes. 3 µL of Spike*-nanobody complex was added to a 300 mesh 1.2/1.3R Au Quantifoil grid previously glow discharged at 15 mA for 30 seconds. Blotting was performed with a blot force of 0 for 4 seconds at 4°C and 100% humidity in a FEI Vitrobot Mark IV (ThermoFisher) prior to plunge freezing into liquid ethane.

For each complex, 120-frame super-resolution movies were collected with a 3x3 image shift collection strategy at a nominal magnification of 105,000x (physical pixel size: 0.834 Å/pix) on a Titan Krios (ThermoFisher) equipped with a K3 camera and a Bioquantum energy filter (Gatan) set to a slit width of 20 eV. Collection dose rate was 8 e^-/pixel/second for a total dose of 66 e^- /$Å^2$. Each collection was performed with semi-automated scripts in SerialEM [46].

Image Processing

For all datasets, dose fractionated super-resolution movies were motion corrected with MotionCor2 [47]. Contrast transfer function determination was performed with cryoSPARC patch CTF [48]. Particles were picked with a 20 Å low-pass filtered apo Spike 2D templates generated from a prior data collection.

Nb6-Spike* and mNb6-Spike* particles were extracted with a 384 pixel box, binned to 96 pixels and subject to single rounds of 2D and 3D classification prior to unbinning for homogenous refinement in cryoSPARC [48]. Refined particles were then imported into Relion3.1 for 3D classification without alignment using the input refinement map low pass filtered to 40 Å [49]. Particles in classes representing the closed conformation of Spike were imported into cisTEM and subject to autorefinement followed by local refinement within a RBD::nanobody masked region [50]. Following local refinement, a new refinement package symmetrized to the C3 axis was created for a final round of local refinement without masking. Final particle counts for each map are as follows: Nb6-Open: 40,125, Nb6-Closed: 58,493, mNb6: 53,690.

Nb11-Spike* particles were extracted with a 512 pixel box, binned to 128 pixels for multiple rounds of 3D classification as described in Figure S4. Following homogenous refinement, particles were exported to Relion3.1. Particle density roughly corresponding to RBD-nanobody complexes was retained post-particle subtraction. 3D classification without alignment was performed on the particle subtracted stacks. Particles in classes with robust RBD-nanobody density were selected, unsubtracted and refined in Relion followed by post-processing. 21,570 particles contributed to the final maps. Final particle counts for each map are as follows: Nb11-Open: 21,570, Nb11-Closed: 27,611. For all maps, final local resolution estimation and GSFSC determination was carried out in cryoSPARC.

Structure modeling

Models of Nb6-Spike* and mNb6-Spike* were built using a previously determined structure of closed Spike* (PDB: 6VXX) [14]. A composite model incorporating resolved regions of the RBD was made using a previously determined X-ray crystal structure of the SARS-CoV-2 RBD (PDB: 6M0J) [51]. For Nb6, the beta2-adrenergic receptor nanobody Nb80 (PDB: 3P0G) was used as a template to first fit the nanobody into the cryo-EM density map for the Nb6-Spike* complex [52]. Complementarity determining loops were then truncated and rebuilt using RosettaES [53]. The final structure was inspected and manually adjusted in COOT and ISOLDE, followed by real space refinement in PHENIX [54-56]. The higher resolution structure of mNb6 enabled manual building of nanobody CDR loops *de novo*, and therefore the Rosetta-based approach was not used for modeling. Final models were analyzed in PHENIX, with statistics reported in Supplementary Table 1.

For models of Nb11-Spike* complexes presented here, the closest nanobody by sequence in the PDB (beta2-adrenergic receptor Nb60, PDB ID: 5JQH) was fit by rigid-body refinement in COOT into the cryo-EM density map using only the framework regions [57]. While the lower resolution of these maps precluded confident assignment of loop conformations, the overall orientation of Nb11 relative to Spike* was well constrained, enabling accurate modeling of distances between the N- and C- termini of two Nb11 molecules bound to Spike*.

Radiolytic hydroxyl radical footprinting and mass-spectrometry of Spike* and Nb3-Spike*

Spike* and Nb3 samples were buffer exchanged into 10 mM phosphate buffer (pH 7.4) by extensive dialysis at 25 °C. A 1.5-fold molar excess of Nb3 was added to 5 μM Spike* and the complex was incubated for >24 hr at 25 °C. For radiolytic footprinting, protein concentrations and beam parameters were optimized using an Alexa-488 fluorophore assay [58]. Apo Spike* and Spike*-Nb3 complex at concentrations of 1-3 μM were exposed to a synchrotron X-ray white beam at 6 timepoints between 0-50 ms at beamline 3.2.1 at the Advanced Light Source in Berkeley, CA and were quenched with 10 mM methionine amide immediately post-exposure. Glycans were removed by treatment with 5% SDS, 5 mM DTT at 95 °C for five minutes and subsequent PNGase (Promega) digestion at 37°C for 2 hours. Samples were buffer exchanged into ammonium bicarbonate (ABC) buffer (pH 8.0) using ZebaSpin columns (Thermo Fisher). Alkylation of cysteines was achieved by treatment with 8 M urea and 5 mM DTT at 37°C for 30 minutes followed by an incubation with 15 mM iodoacetamide at 25 °C in the dark for 30 minutes. All samples were further buffer exchanged to ABC pH 8.0 using ZebaSpin columns

and digested with either Trypsin/Lys-C or Glu-C (Promega) at an enzyme:protein ratio of 1:20 (w/w) at 37 °C for 8 hours.

Samples were lyophilized and resuspended in 1% formic acid at 200 fmol/µL concentration. For each MS analysis, 1 µL of sample was injected onto a 5 mm Thermo Trap C18 cartridge, and then separated over a 15 cm column packed with 1.9 µm Reprosil C18 particles (Dr. Maisch HPLC GmbH) by a nanoElute HPLC (Bruker). Separation was performed at 50 °C and a flow rate of 400 µL/min by the following gradient in 0.1% formic acid: 2% to 17% acetonitrile from 0 to 20 min, followed by 17% to 28% acetonitrile from 20 to 40 min. The eluent was electrospray ionized into a Bruker timsTOF Pro mass spectrometer and data was collected using data-dependent PASEF acquisition. Database searching and extraction of MS1 peptide abundances was performed using the FragPipe platform with either trypsin or GluC enzyme specificity, and all peptide and protein identifications were filtered to a 1% false-discovery rate [59]. Searches were performed against a concatenated protein database of the Spike protein, common contaminant proteins, and the *Saccharomyces cerevisiae* proteome (downloaded July 23, 2020). Note, the *Saccharomyces cerevisiae* proteome was included to generate a sufficient population of true negative identifications for robust false discovery rate estimation of peptide and protein identifications. Lastly, the area under the curve MS1 intensities reported from FragPipe were summarized for each peptide species using MSstats [60].

The peak areas of extracted ion chromatograms and associated side-chain modifications were used to quantify modification at each timepoint. Increasing beamline exposure time decreases the fraction of unmodified peptide and can be represented as a site-specific dose-response plot (Supplementary Fig. 5B). The rate of hydroxyl radical reactivity (k_{fp}) is dependent on both the intrinsic reactivity of each residue and its solvent accessibility and was calculated by fitting the dose-response to a pseudo-first order reaction scheme in Graphpad Prism Version 8. The ratio of k_{fp} between apo Spike* and the Spike-Nb3 complex at specific residues gave information on solvent accessibility changes between the two samples. These changes were mapped onto the SARS-CoV-2 Spike (PDB 6XR8) [11]. In some cases, heavily modified residues show a flattening of dose-response at long exposures which we interpret as radical induced damage. These over-exposed timepoints were excluded from the calculation of k_{fp}.

mNb6 crystallography and structure determination

Purified mNb6 was concentrated to 18.7 mg/mL and filtered using 0.1 µm hydrophilic PVDF filters (Millipore). mNb6 crystal screens were set up in 96 well plates in hanging drop format at 2:1 protein:reservoir in Index and AmSO4 screens (Hampton Research, Aliso Viejo, CA). Crystals in over 60 different screening conditions with various morphologies appeared overnight at ambient temperature and were obtained directly from the screens without further optimization. The crystals were cryoprotected by quick dipping in a solution containing 80% reservoir and 20% PEG400 or 20% Glycerol, then mounted in CrystalCap HT Cryoloops (Hampton Research, Aliso Viejo, CA) and flash cooled in a cryogenic nitrogen stream (100 K). All data were collected at the Advanced Light Source (Berkeley, CA) beam line 8.3.1. A single crystal of mNb6 that grew in 0.1 M Tris.HCl pH 8.5, 1.0 M Ammonium sulfate diffracted to 2.05 Å. Integration, and scaling were performed with Xia2, using XDS for indexing and integration and XSCALE for scaling and merging [61]. The structure was solved molecular replacement using PHASER using the structure of nanobody, Nb.b201 (PDB 5VNV) as search model [45, 62]. Model building was performed with COOT and refined with PHENIX and BUSTER[54, 56, 63].

Pseudovirus assays for nanobody neutralization

ZsGreen SARS-CoV-2-pseudotyped lentivirus was generated according to a published protocol [20]. The day before transduction, 50,000 ACE2 expressing HEK293T cells were plated in each well of a 24-well plate. 10-fold serial dilutions of nanobody were generated in complete medium (DMEM + 10% FBS + PSG) and pseudotyped virus was added to a final volume of 200 µL. Media was replaced with nanobody/pseudotyped virus mixture for four hours, then removed. Cells were washed with complete medium and then incubated in complete medium at 37 °C. Three days post-transduction, cells were trypsinized and the proportion of ZsGreen+ cells was measured on an Attune flow cytometer (ThermoFisher).

Authentic SARS-CoV-2 neutralization assay

SARS-CoV-2, isolate France/IDF0372/2020, was supplied by the National Reference Centre for Respiratory Viruses hosted by Institut Pasteur (Paris, France) and headed by Pr. Sylvie van der Werf. Viral stocks were prepared by propagation in Vero E6 cells in Dulbecco's modified Eagle's medium (DMEM) supplemented with 2% (v/v) fetal bovine serum (FBS, Invitrogen). Viral titers were determined by plaque assay. All plaque assays involving live SARS-CoV-2 were performed at Institut Pasteur Paris (IPP) in compliance with IPP's guidelines following Biosafety Level 3 (BSL-3) containment procedures in approved laboratories. All experiments were performed in at least three biologically independent samples.

Neutralization of infectious SARS-CoV-2 was performed using a plaque reduction neutralization test in Vero E6 cells (CRL-1586, ATCC). Briefly, nanobodies (or ACE2-Fc) were eight-fold serially diluted in DMEM containing 2% (v/v) FBS and mixed with 50 plaque forming units (PFU) of SARS-CoV-2 for one hour at 37°C, 5% CO_2. The mixture was then used to inoculate Vero E6 cells seeded in 12-well plates, for one hour at 37 °C, 5% CO2. Following this virus adsorption time, a solid agarose overlay (DMEM, 10% (v/v) FBS and 0.8% agarose) was added. The cells were incubated for a further 3 days prior to fixation using 4% formalin and plaques visualized by the addition of crystal violet. The number of plaques in quadruplicate wells for each dilution was used to determine the half maximal inhibitory concentrations (IC_{50}) using 3-parameter logistic regression (GraphPad Prism version 8).

Nanobody stability studies

Nanobody thermostability by circular dichroism was assessed using a Jasco J710 CD spectrometer equipped with a Peltier temperature control. Individual nanobody constructs were diluted to 5 μM in phosphate buffered saline. Mollar ellipticity was measured at 204 nm (2 nm bandwidth) between 25 °C and 80 °C with a 1 °C/min heating rate. The resulting molar ellipticity values were normalized and plotted in GraphPad Prism 8.0 after applying a nearest neighbor smoothing function.

For nanobody competition experiments on ACE2 expressing HEK293T cells, nanobodies were incubated at either 25°C or 50°C for one hour. Alternatively, each nanobody was aerosolized with a portable mesh nebulizer producing 2-5 μm particles at a final concentration of 0.5 mg/mL. The resulting aerosol was collected by condensation into a 50 mL tube cooled on ice. Samples were then treated as indicated above to determine IC50 values for binding to Spike*-Alexa647.

Further experiments assessing mNb6 and mNb6-tri stability to aerosolization and lyophilization used a starting concentration of 0.5 mg/mL of each construct. Aerosolization was performed as described above. For lyophilization, nanobodies were first flash frozen in liquid nitrogen and the solution was dried to completion under vacuum. The resulting dried material was resuspended in 20 mM HEPES pH 7.5, 150 mM NaCl. Size exclusion chromatography of the unstressed, post-aerosolization, and post-lyophilization samples were performed an a Superdex 75 Increase 10/300 column in 20 mM HEPES pH 7.5, 150 mM NaCl. SPR experiments to assess binding to Spike* were performed as described above.

Acknowledgements

This work was supported by the UCSF Program for Breakthrough Biomedical Research (PBBR), which is partially funded by the Sandler Foundation. Further support was provided by the National Institutes of Health (NIH) grant DP5OD023048 (A.Manglik). Cryo-EM equipment at UCSF is partially supported by NIH grants S10OD020054 and S10OD021741. Work by M.Vignuzzi was funded by the Laboratoire d'Excellence grant ANR-10-LABX-62-IBEID and the URGENCE COVID-19 Institut Pasteur fundraising campaign. The radiolytic hydroxyl radical footprinting is supported by NIH 1R01GM126218. The Advanced Light Source is supported by the Office of Science, Office of Biological and Environmental Research, of the U.S. DOE under contract DE-AC02-05CH11231. S.Sangwan was supported by a Helen Hay Whitney postdoctoral fellowship. C.Billesbølle acknowledges support from the Alfred Benzon Foundation. K.Leon was funded by NIH/NINDS award F31NS113432 and a UCSF Discovery Fellowship from the Otellini Family. M.Ott acknowledges support through a gift from the Roddenbury Foundation. P.Walter is an Investigator of the Howard Hughes Medical Institute. A.Manglik acknowledges support from the Pew Charitable Trusts, the Esther and A. & Joseph Klingenstein Fund and the Searle Scholars Program.

We thank the entire Walter and Manglik labs for facilitating the development and rapid execution of this large-scale collaborative effort. We thank Sebastian Bernales and Tony De Fougerolles for advice and helpful discussion, and Jonathan Weissman for input into the project and reagent and machine use. We thank Jim Wells for providing the ACE2 ECD-Fc construct, Jason McLellan for providing Spike, RBD, and ACE2 constructs, and Florian Krammer for providing an RBD construct. We thank George Meigs and other Beamline staff at ALS, 8.3.1 for their help in data collection.

QCRG Structural Biology Consortium.

In addition to those listed explicitly in the author contributions, the structural biology portion of this work was performed by the QCRG (Quantitative Biosciences Institute Coronavirus Research Group) Structural Biology Consortium. Listed below are the contributing members of the consortium listed by teams in order of team relevance to the published work. Within each team the team leads are italicized (responsible for organization of each team, and for the experimental design utilized within each team), then the rest of team members are listed alphabetically. *CryoEM grid freezing/collection team: Caleigh M. Azumaya,*

Cristina Puchades, Ming Sun, Julian R. Braxton, Axel F. Brilot, Meghna Gupta, Fei Li, Kyle E. Lopez, Arthur Melo, Gregory E. Merz, Frank Moss, Joana Paulino, Thomas H. Pospiech, Jr., Sergei Pourmal, Alexandrea N. Rizo, Amber M. Smith, Paul V. Thomas, Feng Wang, Zanlin Yu. *CryoEM data processing team: Miles Sasha Dickinson, Henry C. Nguyen*, Daniel Asarnow, Julian R. Braxton, Melody G. Campbell, Cynthia M. Chio, Un Seng Chio, Devan Diwanji, Bryan Faust, Meghna Gupta, Nick Hoppe, Mingliang Jin, Fei Li, Junrui Li, Yanxin Liu, Gregory E. Merz, Joana Paulino, Thomas H. Pospiech, Jr., Sergei Pourmal, Smriti Sangwan, Raphael Trenker, Donovan Trinidad, Eric Tse, Kaihua Zhang, Fengbo Zhou. *Crystallography team: Nadia Herrera, Huong T. Kratochvil, Ursula Schulze-Gahmen, Michael C. Thompson, Iris D. Young*, Justin Biel, Ishan Deshpande, Xi Liu. *Mammalian cell expression team: Christian Bache Billesbølle, Melody G. Campbell, Devan Diwanji, Carlos Nowotny, Amber M. Smith, Jianhua Zhao*, Caleigh M. Azumaya, Alisa Bowen, Nick Hoppe, Yen-Li Li, Phuong Nguyen, Cristina Puchades, Mali Safari, Smriti Sangwan, Kaitlin Schaefer, Raphael Trenker, Tsz Kin Martin Tsui, Natalie Whitis. *Protein purification team: Daniel Asarnow, Michelle Moritz, Tristan W. Owens, Sergei Pourmal*, Caleigh M. Azumaya, Cynthia M. Chio, Amy Diallo, Bryan Faust, Meghna Gupta, Kate Kim, Joana Paulino, Jessica K. Peters, Kaitlin Schaefer, Tsz Kin Martin Tsui. *Bacterial expression team: Amy Diallo, Meghna Gupta*, *Erron W. Titus*, Jenny Chen, Roberto Efraín Díaz, Loan Doan, Sebastian Flores, Mingliang Jin, Huong T. Kratochvil, Victor L. Lam, Yang Li, Megan Lo, Gregory E. Merz, Joana Paulino, Aye C. Thwin, Stephanie Wankowicz, Zanlin Yu, Yang Zhang, Fengbo Zhou. *Infrastructure team:* David Bulkley, Arceli Joves, Almarie Joves, Liam McKay, Mariano Tabios, Eric Tse. *Leadership team: Oren S Rosenberg, Kliment A Verba*, David A Agard, Yifan Cheng, James S Fraser, Adam Frost, Natalia Jura, Tanja Kortemme, Nevan J Krogan, Aashish Manglik, Daniel R. Southworth, Robert M Stroud. The QCRG Structural Biology Consortium has received support from: Quantitative Biosciences Institute, Defense Advanced Research Projects Agency HR0011-19-2-0020 (to D.A.Agard and K.A.Verba; B. Shoichet PI), FastGrants COVID19 grant (K.A.Verba PI), Laboratory For Genomics Research (O.S.Rosenberg PI) and Laboratory for Genomics Research LGR-ERA (R.M.Stroud PI). R.M.Stroud is supported by NIH grants AI 50476, GM24485.

Author Contributions

M.Schoof purified Spike*, RBD, and ACE2 proteins, performed yeast display selections to identify and affinity mature nanobodies, expressed and purified nanobodies, tested activity in cell-based assays, cloned, expressed, and purified multivalent nanobody constructs, and

coordinated live virus experiments. B.Faust purified and characterized Spike* protein and candidate nanobodies, developed, performed and analyzed SPR experiments for Spike* and RBD-nanobody affinity determination, developed, performed and analyzed SPR binning, experiments, determined optimal freezing conditions for cryo-EM experiments, processed, refined and generated figures for Nb6, Nb11, and mNb6 EM datasets. R.Saunders expressed and purified ACE2 and nanobodies, developed and performed cell-based assays for inhibition of Spike* binding and pseudovirus assays for determining nanobody efficacy. S.Sangwan expressed and purified Spike*, RBD, ACE2-Fc, and nanobodies, processed cryo-EM data, optimized RBD-nanobody complexes for crystallography, grew crystals of mNb6, collected diffraction data, and refined the X-ray crystal structure of mNb6. V.Rezelj tested efficacy of nanobody constructs in live SARS-CoV-2 infection assays under the guidance of M.Vignuzzi. N.Hoppe purified nanobodies, developed, performed and analyzed SPR binning experiments, developed performed and analyzed variable Nb6-bi and Nb6-tri association experiments, and performed thermal melting stability assays for nanobody constructs. M.Boone developed approaches to express and purify nanobodies from *Pichia pastoris* and developed, performed, and analyzed approaches to quantify nanobody efficacy in live virus assays. C.Azumaya and C.Puchades determined optimal freezing conditions for cryo-EM experiments with B.Faust, optimized data collection approaches, and collected cryo-EM datasets. C.B.Billesbølle expressed and purified Spike*, generated affinity maturation library for Nb6, and performed yeast display selections to identify mNb6. I.Deshpande expressed and purified nanobody constructs. J.Liang and C.B.Billesbølle built the yeast nanobody library enabling discovery of nanobodies in this study. B.Zha. performed live SARS-CoV-2 virus assays to test nanobody efficacy with guidance from O.Rosenberg. C.R.Simoneau and K.Leon performed live SARS-CoV-2 virus assays to test nanobody efficacy with guidance from M.Ott. K.M.White performed live SARS-CoV-2 virus assays to test nanobody efficacy with guidance from A.Garcia-Sastre. A.W.Barile-Hill performed SPR experiments with B.Faust. A.A.Anand, N.Dobzinski, B.Barsi-Rhyne, and Y.Liu. assisted in cloning, expression, and purification of nanobody and pseudovirus constructs. V.Belyy perfomed single-molecule nanobody-Spike* interaction studies. S.Nock prepared media and coordinated lab usage during UCSF's partial shutdown. M.Zimanyi and S.Gupta performed radiolytic footprinting experiments with guidance from C.Ralston and analyzed mass spectrometry data generated by D.L.Swaney. Several members of the QCRG Structural Biology Consortium played an exceptionally important role for this project. A.Rizo, A.Smith, F.Moss collected cryo-EM data on Spike*-nanobody complexes. S.Dickinson, H.Nguyen, K.Verba, C. Chio, U.S.Chio, M.Gupta, M.Jin, F.Li, Y.Liu, G.Merz, K.Zhang analyzed

cryo-EM data from 15 Spike*-nanobody complex datasets. H.Kratochvil set up crystallization trials of various RBD-nanobody complexes, and crystallized, collected diffraction data for, and refined the mNb6 structure. M.Thompson collected, processed, and refined the mNb6 structure. D.Devanji and K.Schaefer expressed and purified Spike*. A.Manglik expressed and purified Spike*, labeled Spike* for biochemical studies, designed selection strategies for nanobody discovery, cloned nanobodies for expression, designed affinity maturation libraries and performed selections, analyzed SPR data, and performed nanobody stability studies. The overall project was supervised by P.Walter and A.Manglik.

Competing Interests

M.Schoof, B.Faust, R.Saunders, N.Hoppe, P.Walter, and A.Manglik are inventors on a provisional patent describing anti-Spike nanobodies described in this manuscript.

REFERENCES

1. Ksiazek, T.G., et al., *A novel coronavirus associated with severe acute respiratory syndrome.* N Engl J Med, 2003. **348**(20): p. 1953-66.
2. Zaki, A.M., et al., *Isolation of a novel coronavirus from a man with pneumonia in Saudi Arabia.* N Engl J Med, 2012. **367**(19): p. 1814-20.
3. Zhou, P., et al., *A pneumonia outbreak associated with a new coronavirus of probable bat origin.* Nature, 2020. **579**(7798): p. 270-273.
4. Chan, J.F., et al., *A familial cluster of pneumonia associated with the 2019 novel coronavirus indicating person-to-person transmission: a study of a family cluster.* Lancet, 2020. **395**(10223): p. 514-523.
5. Huang, C., et al., *Clinical features of patients infected with 2019 novel coronavirus in Wuhan, China.* Lancet, 2020. **395**(10223): p. 497-506.
6. Wu, F., et al., *A new coronavirus associated with human respiratory disease in China.* Nature, 2020. **579**(7798): p. 265-269.
7. Zhu, N., et al., *A Novel Coronavirus from Patients with Pneumonia in China, 2019.* N Engl J Med, 2020. **382**(8): p. 727-733.
8. World Health Organization. *WHO Coronavirus Disease (COVID-19) Dashboard*. 2020; Available from: https://covid19.who.int/.
9. Ke, Z., et al., *Structures, conformations and distributions of SARS-CoV-2 spike protein trimers on intact virions.* bioRxiv, 2020: p. 2020.06.27.174979.
10. Bosch, B.J., et al., *The coronavirus spike protein is a class I virus fusion protein: structural and functional characterization of the fusion core complex.* J. Virol., 2003. **77**(16): p. 8801-8811.
11. Cai, Y., et al., *Distinct conformational states of SARS-CoV-2 spike protein.* Science, 2020.
12. Wang, Q., et al., *Structural and Functional Basis of SARS-CoV-2 Entry by Using Human ACE2.* Cell, 2020. **181**(4): p. 894-904.e9.
13. Yan, R., et al., *Structural basis for the recognition of SARS-CoV-2 by full-length human ACE2.* Science, 2020. **367**(6485): p. 1444-1448.
14. Walls, A.C., et al., *Structure, Function, and Antigenicity of the SARS-CoV-2 Spike Glycoprotein.* Cell, 2020. **181**(2): p. 281-292.e6.
15. Wrapp, D., et al., *Cryo-EM structure of the 2019-nCoV spike in the prefusion conformation.* Science, 2020. **367**(6483): p. 1260-1263.
16. Hoffmann, M., et al., *SARS-CoV-2 Cell Entry Depends on ACE2 and TMPRSS2 and Is Blocked by a Clinically Proven Protease Inhibitor.* Cell, 2020. **181**(2): p. 271-280.e8.
17. Shang, J., et al., *Structural basis of receptor recognition by SARS-CoV-2.* Nature, 2020. **581**(7807): p. 221-224.
18. Gupta, S., et al., *Synchrotron X-ray footprinting as a method to visualize water in proteins.* J Synchrotron Radiat, 2016. **23**(Pt 5): p. 1056-69.
19. Zhang, Y., et al., *Mapping the Binding Interface of VEGF and a Monoclonal Antibody Fab-1 Fragment with Fast Photochemical Oxidation of Proteins (FPOP) and Mass Spectrometry.* J Am Soc Mass Spectrom, 2017. **28**(5): p. 850-858.
20. Crawford, K.H.D., et al., *Protocol and Reagents for Pseudotyping Lentiviral Particles with SARS-CoV-2 Spike Protein for Neutralization Assays.* Viruses, 2020. **12**(5).
21. Kunz, P., et al., *The structural basis of nanobody unfolding reversibility and thermoresistance.* Sci Rep, 2018. **8**(1): p. 7934.
22. Baum, A., et al., *Antibody cocktail to SARS-CoV-2 spike protein prevents rapid mutational escape seen with individual antibodies.* Science, 2020.
23. Cao, Y., et al., *Potent Neutralizing Antibodies against SARS-CoV-2 Identified by High-Throughput Single-Cell Sequencing of Convalescent Patients' B Cells.* Cell, 2020. **182**(1): p. 73-84.e16.

24. Chi, X., et al., *A neutralizing human antibody binds to the N-terminal domain of the Spike protein of SARS-CoV-2.* Science, 2020.
25. Ju, B., et al., *Human neutralizing antibodies elicited by SARS-CoV-2 infection.* Nature, 2020.
26. Liu, L., et al., *Potent neutralizing antibodies directed to multiple epitopes on SARS-CoV-2 spike.* Nature, 2020.
27. Pinto, D., et al., *Cross-neutralization of SARS-CoV-2 by a human monoclonal SARS-CoV antibody.* Nature, 2020. **583**(7815): p. 290-295.
28. Rogers, T.F., et al., *Isolation of potent SARS-CoV-2 neutralizing antibodies and protection from disease in a small animal model.* Science, 2020.
29. Zost, S.J., et al., *Potently neutralizing and protective human antibodies against SARS-CoV-2.* Nature, 2020.
30. Leyva-Grado, V.H., et al., *Direct administration in the respiratory tract improves efficacy of broadly neutralizing anti-influenza virus monoclonal antibodies.* Antimicrob Agents Chemother, 2015. **59**(7): p. 4162-72.
31. Detalle, L., et al., *Generation and Characterization of ALX-0171, a Potent Novel Therapeutic Nanobody for the Treatment of Respiratory Syncytial Virus Infection.* Antimicrob Agents Chemother, 2016. **60**(1): p. 6-13.
32. Wrapp, D., et al., *Structural Basis for Potent Neutralization of Betacoronaviruses by Single-Domain Camelid Antibodies.* Cell, 2020. **181**(5): p. 1004-1015.e15.
33. Huo, J., et al., *Neutralizing nanobodies bind SARS-CoV-2 spike RBD and block interaction with ACE2.* Nat. Struct. Mol. Biol., 2020.
34. Walter, J.D., et al., *Sybodies targeting the SARS-CoV-2 receptor-binding domain.* bioRxiv, 2020.
35. Sun, Z., et al., *Potent neutralization of SARS-CoV-2 by human antibody heavy-chain variable domains isolated from a large library with a new stable scaffold.* MAbs, 2020. **12**(1): p. 1778435.
36. Wu, Y., et al., *Identification of Human Single-Domain Antibodies against SARS-CoV-2.* Cell Host Microbe, 2020. **27**(6): p. 891-898.e5.
37. Esparza, T.J. and D.L. Brody, *High Affinity Nanobodies Block SARS-CoV-2 Spike Receptor Binding Domain Interaction with Human Angiotensin Converting Enzyme.* bioRxiv, 2020: p. 2020.07.24.219857.
38. Hanke, L., et al., *An alpaca nanobody neutralizes SARS-CoV-2 by blocking receptor interaction.* bioRxiv, 2020: p. 2020.06.02.130161.
39. Custódio, T.F., et al., *Selection, biophysical and structural analysis of synthetic nanobodies that effectively neutralize SARS-CoV-2.* bioRxiv, 2020: p. 2020.06.23.165415.
40. Li, T., et al., *Potent synthetic nanobodies against SARS-CoV-2 and molecular basis for neutralization.* bioRxiv, 2020: p. 2020.06.09.143438.
41. Nieto, G.V., et al., *Fast isolation of sub-nanomolar affinity alpaca nanobody against the Spike RBD of SARS-CoV-2 by combining bacterial display and a simple single-step density gradient selection.* bioRxiv, 2020: p. 2020.06.09.137935.
42. Chi, X., et al., *Humanized Single Domain Antibodies Neutralize SARS-CoV-2 by Targeting Spike Receptor Binding Domain.* bioRxiv, 2020: p. 2020.04.14.042010.
43. Stadlbauer, D., et al., *SARS-CoV-2 Seroconversion in Humans: A Detailed Protocol for a Serological Assay, Antigen Production, and Test Setup.* Curr. Protoc. Microbiol., 2020. **57**(1): p. e100.
44. Lui, I., et al., *Trimeric SARS-CoV-2 Spike interacts with dimeric ACE2 with limited intra-Spike avidity.* bioRxiv, 2020: p. 2020.05.21.109157.
45. McMahon, C., et al., *Yeast surface display platform for rapid discovery of conformationally selective nanobodies.* Nat. Struct. Mol. Biol., 2018. **25**(3): p. 289-296.

46. Mastronarde, D.N., *Automated electron microscope tomography using robust prediction of specimen movements.* J Struct Biol, 2005. **152**(1): p. 36-51.
47. Zheng, S.Q., et al., *MotionCor2: anisotropic correction of beam-induced motion for improved cryo-electron microscopy.* Nat Methods, 2017. **14**(4): p. 331-332.
48. Punjani, A., et al., *cryoSPARC: algorithms for rapid unsupervised cryo-EM structure determination.* Nat Methods, 2017. **14**(3): p. 290-296.
49. Zivanov, J., et al., *New tools for automated high-resolution cryo-EM structure determination in RELION-3.* Elife, 2018. **7**.
50. Grant, T., A. Rohou, and N. Grigorieff, *cisTEM, user-friendly software for single-particle image processing.* Elife, 2018. **7**.
51. Lan, J., et al., *Structure of the SARS-CoV-2 spike receptor-binding domain bound to the ACE2 receptor.* Nature, 2020. **581**(7807): p. 215-220.
52. Rasmussen, S.G., et al., *Structure of a nanobody-stabilized active state of the β(2) adrenoceptor.* Nature, 2011. **469**(7329): p. 175-80.
53. Frenz, B., et al., *RosettaES: a sampling strategy enabling automated interpretation of difficult cryo-EM maps.* Nat Methods, 2017. **14**(8): p. 797-800.
54. Emsley, P. and K. Cowtan, *Coot: model-building tools for molecular graphics.* Acta Crystallogr D Biol Crystallogr, 2004. **60**(Pt 12 Pt 1): p. 2126-32.
55. Croll, T.I., *ISOLDE: a physically realistic environment for model building into low-resolution electron-density maps.* Acta Crystallogr D Struct Biol, 2018. **74**(Pt 6): p. 519-530.
56. Adams, P.D., et al., *PHENIX: a comprehensive Python-based system for macromolecular structure solution.* Acta Crystallogr D Biol Crystallogr, 2010. **66**(Pt 2): p. 213-21.
57. Staus, D.P., et al., *Allosteric nanobodies reveal the dynamic range and diverse mechanisms of G-protein-coupled receptor activation.* Nature, 2016. **535**(7612): p. 448-52.
58. Gupta, S., et al., *The Beamline X28C of the Center for Synchrotron Biosciences: a national resource for biomolecular structure and dynamics experiments using synchrotron footprinting.* J Synchrotron Radiat, 2007. **14**(Pt 3): p. 233-43.
59. Yu, F., et al., *Fast quantitative analysis of timsTOF PASEF data with MSFragger and IonQuant.* Mol Cell Proteomics, 2020.
60. Choi, M., et al., *MSstats: an R package for statistical analysis of quantitative mass spectrometry-based proteomic experiments.* Bioinformatics, 2014. **30**(17): p. 2524-6.
61. Kabsch, W., *Automatic processing of rotation diffraction data from crystals of initially unknown symmetry and cell constants.* Journal of Applied Crystallography, 1993. **26**(6): p. 795-800.
62. McCoy, A.J., et al., *Phaser crystallographic software.* J Appl Crystallogr, 2007. **40**(Pt 4): p. 658-674.
63. Bricogne G., B.E., Brandl M., Flensburg C., Keller P., Paciorek W., and S.A. Roversi P, Smart O.S., Vonrhein C., Womack T.O. , *BUSTER version 1.10.0. .* Cambridge, United Kingdom: Global Phasing Ltd., 2017.